7-19-2017

An Experimental Study on Pool Boiling Performance Enhancement and Effect of Aging

Aniket M. Rishi
amr6756@rit.edu

R.I.T

An Experimental Study on Pool Boiling Performance Enhancement and Effect of Aging

by

Aniket M. Rishi

A Thesis Submitted in Partial Fulfillment of the Requirement for the Degree of Master of Science in Mechanical Engineering

Thermal Analysis, Microfluidics, and Fuel Cell Lab

Department of Mechanical Engineering

Kate Gleason College of Engineering

ROCHESTER INSTITUTE OF TECHNOLOGY

Rochester, NY 14623

July 19th, 2017

An Experimental Study on Pool Boiling Performance Enhancement and Effect of Aging

by: Aniket M. Rishi

A Thesis Submitted in Partial Fulfillment of the Requirements for the Degree of Master of Science in Mechanical Engineering

Department of Mechanical Engineering

Kate Gleason College of Engineering

Rochester Institute of Technology

Approved By:

Dr. Satish G. Kandlikar
Thesis Advisor *Date*
Department of Mechanical Engineering

Dr. Anju Gupta
Thesis Co-Advisor *Date*
Department of Chemical Engineering

Dr. Agamemnon Crassidis
Department Representative, Thesis Committee Member *Date*
Department of Mechanical Engineering

Dr. Surendra Gupta
Thesis Committee Member *Date*
Department of Mechanical Engineering

Dr. Michael Schertzer
Thesis Committee Member *Date*
Department of Mechanical Engineering

Acknowledgement

I would like to express my sincere gratitude to Dr. Kandlikar for giving me this great opportunity to work in the Thermal Analysis, Microfluidics, and Fuel Cell Laboratory. Without his continuous support and guidance, this work would not have been possible. I would also like to thank Dr. Anju Gupta for giving me a huge support and motivation for this work. The confidence that you have shown in my work has encouraged me to deliver the best performance.

I would like to specially thank Dr. Surendra Gupta for giving me the training on XRD and for assisting me in this study. As his teaching assistant, I benefited from his teaching skills and systematic problem solving techniques. I would like to thank my committee members Dr. Schertzer and Dr. Surendra Gupta for taking time to review and evaluate my thesis work. I am also thankful to Dr. Crassidis for advising and helping me during my graduate studies at RIT. All the Thermal Analysis, Microfluidics, and Fuel Cell Laboratory members have been really helpful and have constantly encouraged me and trained me. I am really thankful to them for all the things they have done.

Finally, I would like to thank my parents and my brother for their continuous support, encouragement and for showing the confidence in me. Thank you for making all the sacrifices and giving me the opportunity to have this wonderful experience. I would like to thank my brother for providing me everything that I needed. I would also like to thank my girlfriend Sharvari for being there all the time, for being a closest friend and constantly supporting me throughout the journey. You all are my support system. I would also like to thank all my friends for all the support.

Abstract

The miniaturization of electronic devices requires advanced thermal management techniques. The two-phase heat transfer process offers more effective and sustainable approach compared to the presently used single-phase cooling techniques. The boiling heat transfer is a two-phase cooling technique, that dissipates a high heat flux while maintaining the low surface temperature thereby, offering an efficient heat transfer mechanism compared to the single-phase process. Furthermore, the surface enhancement techniques such as micro/nano porous coatings help to maintain the low surface temperature thus improving the overall heat transfer performance. Electrodeposition is a simple technique that enhances this performance by creating the porous structure on the surface. This research focuses on developing an enhanced microscale structures on plain copper surfaces to improve the pool boiling performance. Additionally, the longevity (or the long-term stability) and aging of these enhanced structures, and their effects on the pool-boiling performance is also investigated.

Initially the pool boiling performance of enhanced surfaces is studied. The enhanced surfaces were prepared using electrodeposition of copper and graphene oxide. Later, the effects of repetitive boiling on the morphology of the surfaces were examined using various characterization techniques such as Scanning Electron Microscope (SEM), X-Ray Diffraction (XRD), and Fourier Transform Infrared (FTIR).

The chips coated with electrodeposition method rendered a high pool boiling performance for GS-4 (2.5% GO-Cu electrodeposited chip) with CHF of 220 W/cm² at wall superheat of 14°C, giving ~76% improvement in CHF compared to plain copper chip. While, copper

on copper electrodeposited chip, deposited with a different technique, performs better in both CHF and aging. CHF of 192 W/cm² at wall superheat of 18.8°C was achieved for copper electrodeposited chip, giving ~30% enhancement compared to literature and ~54% enhancement when compared to plain copper chip.

Moreover, surface characterization techniques including Scanning Electron Microscope (SEM) with Energy- Dispersive X-Ray Spectroscopy (EDS), Fourier Transform Infrared (FTIR), and X-Ray Diffraction (XRD) were employed to study the morphologies, elemental species, and to confirm the presence of graphene and graphene oxide on the test surfaces.

Table of Contents

List of figures

List of tables

Nomenclature

Heater surface temperature	T_s
Wall superheat	$\Delta T_{sat}=T_{wall}-T_{sat}$
Heat flux per unit area	q''
Heat transfer coefficient	h
Surface tension	σ
Specific heat of liquid	$c_{p,l}$
Specific heat of vapor	$c_{p,v}$
Specific volume of vapor	ν_v
Specific volume of liquid	ν_l
Receding contact angle	θ_r
Saturation pressure	P_{sat}
Saturation temperature	T_{sat}
Latent heat of vaporization	h_{lv}
Density of liquid	ρ_l
Density of vapor	ρ_v
Dynamic viscosity of vapor	μ_v
Thermal conductivity of liquid	k_l
Thermal conductivity of vapor	k_v

Chapter 1

This chapter provides the framework and the motivation for the current research work and background information on the pool boiling curve, bubble nucleation phenomenon in boiling and the electrochemical principles involved in generation of the graphene-rich surfaces investigated in this study.

1.1 Introduction:

Heat transfer is the most important phenomenon for any heat dissipating device. To maintain the desired functioning of the devices, efficient cooling system is essential. Innovations in miniaturized electronic industry have resulted in multifunctional compact devices with a growing challenge of fire hazards arising from overheating of these devices. There is a growing need of novel systems capable of dissipating the heat in these devices. Cooling can be achieved by two ways, either air cooling or liquid cooling. Since air cooling does not involve phase change, it has limited heat transfer capabilities. In liquid cooling, large amount of heat is absorbed while changing the phase from liquid to gas. Boiling heat transfer is of two types, viz. pool boiling and flow boiling. In pool boiling heat transfer, a pool of the fluid is held stationary while the natural convection causes the heat transfer. Whereas, in a flow boiling system, forced convection progenerates the heat transfer. Fig. 1 shows the range of heat transfer coefficients for single phase and two phase cooling for air and water. To meet the high demands of electronics cooling, two phase cooling system is required due to its high capabilities to transfer the heat.

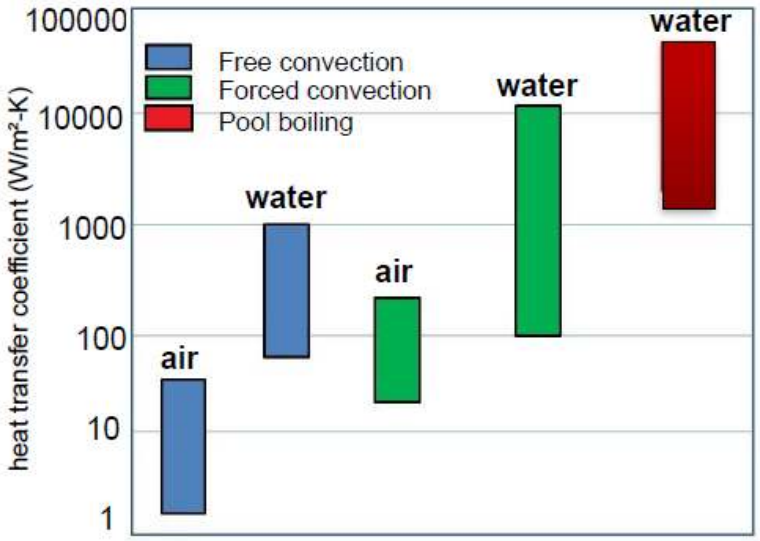

Figure 1: Heat transfer coefficients for single and two phase cooling [1]

Pool boiling is one of the most important phenomenon in which the heat transfer occurs at low wall superheats without the involvement of any no moving parts such as pumps, in the system. In order to improve the pool boiling performance further, several surface enhancement strategies have been investigated, such as micro porous, nanoporous coatings, nano structures, wire frame structures, and micro channels that produce additional nucleation sites. The use of nanofluids has also been shown to advance the heat transfer performance. [2] To understand the heat dissipation using boiling, it is essential to understand the pool boiling curve. A characteristic pool boiling curve is plotted with the heat flux on y-axis and wall superheat on x-axis. The value by which the Critical Heat Flux (CHF) increases and the degree by which the curve shifts to the left represents the enhancement compared to a flat surface.

1.2 Pool Boiling Curve

Pool boiling curve is the most fundamental curve that describes the four different stages of the mechanisms underlying the pool boiling phenomenon as shown in Figure 2 The Y-axis represents the heat flux (q", W/m^2) and the wall superheat (ΔT_{sat}) is designated to the X-axis. The 4 regimes of the plot are described below:

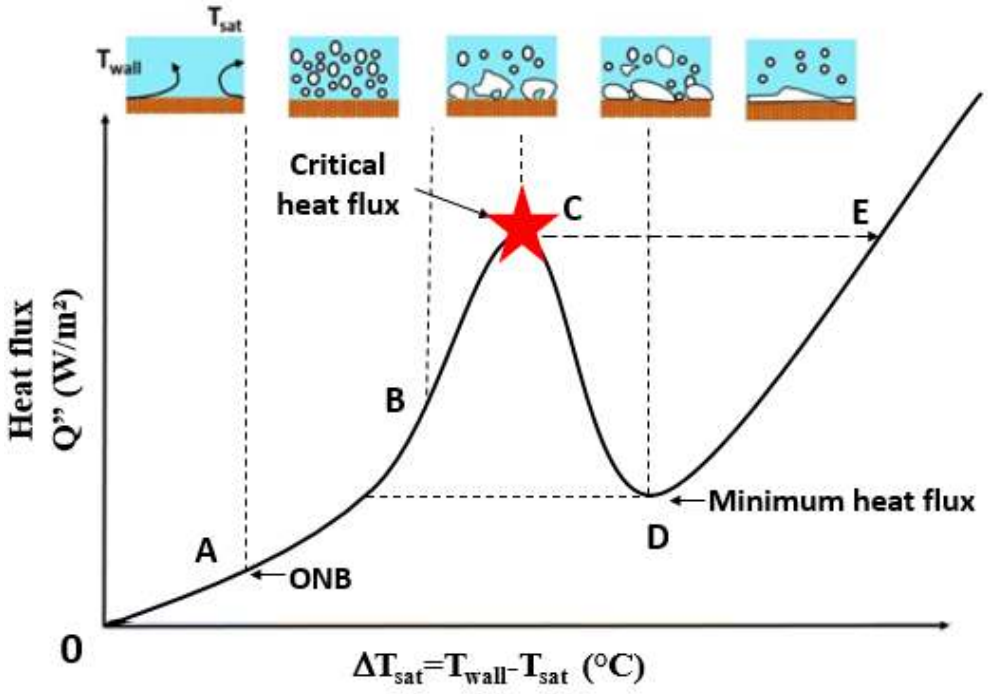

Figure 2: Pool boiling curve

1.2.1 Free convection boiling- natural convection process

When the wall superheat is low, the heat is transferred from heated surface to bulk liquid by the means of natural convection. There are no bubbles in this stage. When this temperature difference rises to a certain value corresponding to point 'A', small vapor bubbles are observed on few sites of the surface. Till point A heat transfer that is occurred

in the liquid is by natural convection current, and the movement of liquid is due to the density variation.

1.2.2 Nucleate boiling- heat dissipation by bubbles

Once nucleation is initiated, under the right conditions, the bubbles grow and nucleate from the heater surface and rise to the free surface in liquid phase shown as the nucleate boiling region in Figure 2. The point when the very first bubble appears on the surface embodies the is onset of the nucleate boiling phase. As the temperature rises beyond point B, additional nucleation sites become active and the rate of generation of bubbles increases. Formation of the bubbles gradually increase at these various nucleation sites carrying the heat to the free surface of liquid.

This rate of formation of bubbles increases rapidly, which in turn increases the heat dissipation rate significantly till point C, at this point; heat flux reaches the maximum value and is known as the Critical Heat Flux (CHF) which indicates the maximum heat that can be dissipated. This section from A to B comes under the nucleate boiling region. [3]

1.2.3 Transition boiling- Insulation layer of vapor

Beyond point C, the bubble generation rate is much higher than the bubble detachment rate. The bubbles formed in this stage, start to combine and form a layer of vapor film in horizontal direction on the surface that prevents any liquid to come in contact with the surface. The vapor film acts as an insulation layer causing the heat flux to reduce rapidly. Under these conditions, the surface temperature may fluctuate rapidly. Since the boiling in

this region is the combination of unstable film boiling and nucleate boiling, it is called as the transition boiling.

1.2.4 Film boiling- Heat transfer due to radiation

In the region, D to E, there is a thin film of vapor covering the heater surface completely. At this stage, heat transfer takes place by conduction and radiation from the wall through the vapor film. This vapor film does not wet the heater surface, although some transient wetting can occur and there can be a formation of bubbles at some regions and at the free interface evaporation occurs, the bubbles then depart from the interface and rise up through the liquid pool. Because the heat transfer in region occurs through the vapor film, this stage is called as film boiling. [4]

1.3 Bubble nucleation

Bubble nucleation occurs when the heated surface or the test surface in a pool boiling experiment is at higher temperature than that of the saturation temperature of the bulk fluid above it.

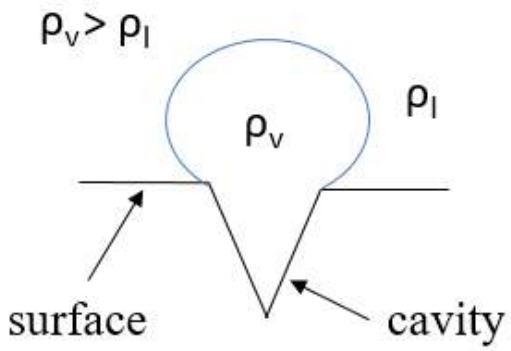

Figure 3: Nucleation of bubble

Figure 3 shows the various forces acting on the bubble. The two forces that act on the bubble are pressure force and surface tension force. The vapor pressure inside the bubble is given by,

$$\rho_V = \rho_l + \frac{2\sigma}{R} \tag{1}$$

Where, ρ_V is vapor pressure inside the bubble,

ρ_l is the pressure of the fluid

σ is the surface tension of the fluid and

R is the radius of the bubble.

From the equation, it is seen that vapor pressure is inversely proportional to the radius of the bubble. [5] Therefore, even for the nucleation of smaller bubble, higher vapor pressure will be required, which indicates that surface temperature should be higher than the fluid temperature.

$$\{r_{cmax}, r_{cmin}\} = \frac{\delta_t \sin\theta_r}{2.2}\left(\frac{\Delta T_{sat}}{\Delta T_{sat} + \Delta T_{sub}}\right)\left[1 \pm \sqrt{1} - \frac{8.8\sigma T_{sat}\,(\Delta T_{sat} + \Delta T_{sub})}{\rho_V h_{lv} \delta_t {T_{sat}}^2}\right] \tag{2}$$

The equation above determines the range of radii of the cavity for nucleation. This implies that the cavities lying within this range will act as a nucleation site. The cavities are also dependent of the surface finish. For a very smooth and polished surface, higher wall superheat temperatures are required and this required high wall superheat is given by, [5]

$$\Delta T_{sat,ONB\ at\ r_c} = \frac{1.1 r_c q''}{k_l \sin\theta_r} + \frac{2\sigma \sin\theta_r T_{sat}}{r_c \rho_v h_{lv}} \tag{3}$$

1.4 Electrodeposition Technique

Electrochemical deposition is the process of coating on a base material to modify the surface properties. Electrochemical cell is the device where these chemical reactions occur. Electrochemical cell consists of electrolyte and the electrode as the main components. Electrode is an electronic conductor through which the current flows by the movements of electrons. Electrochemical cell consists of two electrodes; working electrode and counter electrode. Working electrode is the electrode where the reaction of interest occurs and a source of this deposition is the counter electrode. The electrolyte is the medium that allows for the charge transportation between the working and counter electrodes by the means of ionic movement. When these two electrodes are connected to power supply, current flows from counter electrode to working electrode. The atomic particles of counter electrode flow through electrolyte and get deposited on working electrode. Since, current always flow from anode to cathode, hence, counter electrode acts as anode and working electrode acts as cathode. [6]

Electrodeposition or electroplating is used in number of applications including mechanical, automotive and metallurgical industries, and micro or nanotechnologies. It also helps to achieve desired electrical and corrosion resistance, or electrical conductance, improved heat tolerance. [7] Electrodeposition coating technique has also been used to create microporous coatings on boiling test surfaces . [8] [9]

Shin and Liu [10] used the electrodeposition method to create the surfaces. They observed that the porous size of the surface increased with increase in time of the deposition. Also, the porosity is increased with increase in evolution of hydrogen bubbles and can be

controlled by controlling the percentage of concentrated sulphuric acid. But, the deposited structure came off during the pool boiling tests as reported by Patil and Kandlikar [11] and hence bonding is the important issue to get the stable results.

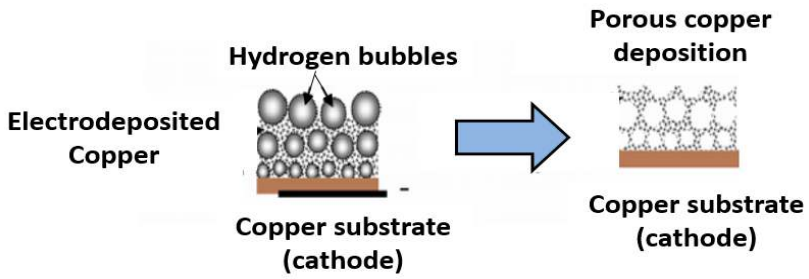

Figure 4: Evolution of hydrogen bubbles forming porous surface

Albertson [12] proposed a technique in which deposition is obtained by initially coating at higher current densities for a short duration, and lower current densities for a longer duration. In the first step, deposition of copper along with simultaneous evolution of hydrogen bubbles occurs, leaving behind porous copper as shown in figure 15. In the second step, the current density is taken such that the copper is deposited without evolution of hydrogen. This improves the bonding and the porosity of the copper surface. Hence, this method is used to create the micro porous surfaces.

1.5 Graphene and graphene oxide

Graphene is a tightly packed layer of carbon atoms which are bonded together in a hexagonal lattice in a honeycomb like structure. In other words, graphene is a two-dimensional form of graphite. Graphene has very phenomenal properties including highest strength and very high thermal conductivity. Thermal conductivity of graphene is in the range of 4800 to 5300 W/m K. [13] Graphene is the thinnest material available yet having very high strength. Due to its unique properties, graphene has several applications in the field of composites and coating, energy, electronics, heat transfer, biomedical and many more. [14]

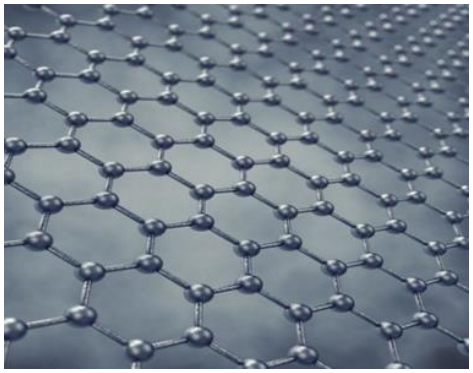

Figure 5: 2D hexagonal structure of graphene

1.6 Goals of the current work

Boiling heat transfer approach is very efficient and has massive advantages compared to conventional air cooling techniques. It can serve as a potential cooling method for large data centers, highly powered electronic components and systems, boilers, heat exchangers, and nuclear reactors. In order to enhance the performance of two phase cooling further, the

test surface should dissipate the large amount of heat by keeping its temperature to the minimum value while, establishing a high heat transfer coefficient of the surface. Hence the main goals of this work are to i) improve the CHF of the test surface and ii) keep the wall superheat temperature to a minimum value, iii) improve the aging of the electrodeposited surfaces, and improve the pool boiling performance of the aged test surface than the plain test surface.

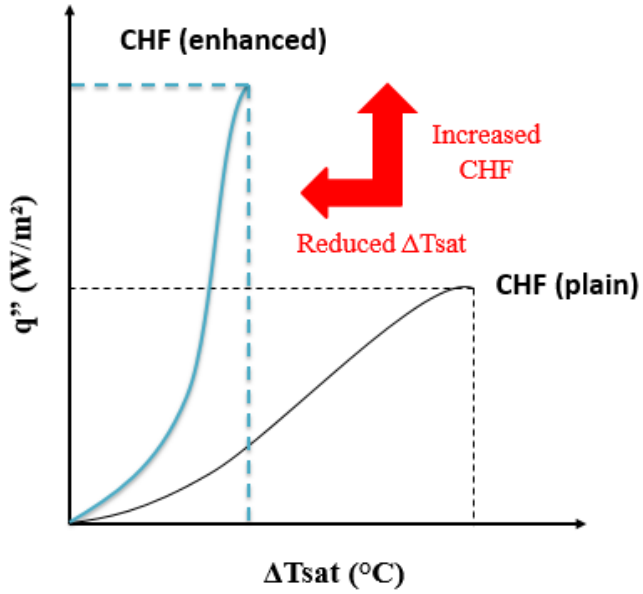

Figure 6: Desired Goals of pool boiling enhancement

Chapter 2

This chapter covers a detailed literature review on different surface enhancement techniques, performance of heat transfer surfaces with porous media, and the mechanisms involved for the enhancements in boiling heat transfer.

2.1 Literature review

Literature review is divided in two different sections – a) the various enhancement techniques that includes microporous surfaces and their wettability, and electrodeposition of carbon based coatings, and b) the mechanisms involved in the increase in pool boiling performance. Sections include the enhancement based on.

2.1.1 Enhanced heat transfer – microporous surfaces

Pool boiling performance of the micro porous surfaces has been reported extensively. Porous surfaces have higher heat flux at low wall superheat due to increased surface area and nucleation sites. To be effectively tested for the pool boiling testing, bond strength of the porous surface must be strong enough such that the coating should not come off. Bargles and Chyu [9] demonstrated that a steady vapor formation takes place on the porous media and the nucleation takes place within the matrix via the re-entrant cavities that are not susceptible to flooding by liquid. When the heat is supplied to the heater surface, nucleus of a bubble grows in the cavity. When this bubble nucleates, it carries heat with itself. As the bubble departs, the liquid in the vicinity of void fills the cavity, thus

there is continuous supply of fluid for the evaporation. Higher the nucleation frequency, higher the heat dissipated from the surface. [10]

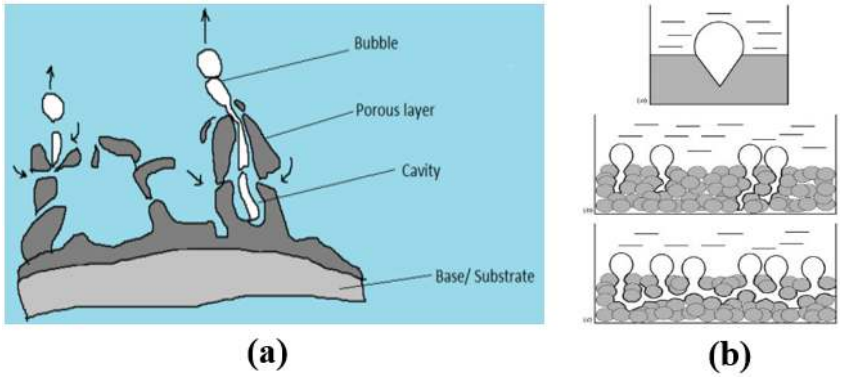

Figure 7: (a) Microporous surface, (b) Boiling mechanism in porous surface *[16]*

Mori and Okuyama [17] enhanced CHF by the attachment of a honeycomb structured porous plate with different thickness (1.2 mm, 5 mm, 10 mm) on a heated surface. As the thickness of the honeycomb porous plate on the heated surface decreased, the CHF increased to 250 W/cm^2. They found that the self-regulated liquid supply due to capillary action and reduction of flow resistance to liquid and vapor flow improved the heat transfer. Patil and Kandlikar [11] reviewed several ways to form porous surfaces for boiling heat transfer by investigating Three main manufacturing techniques that are commonly used for creating porous boiling surfaces include- sintering, electrodeposition, and advanced techniques such as vapor blasting, jet impingement, spray coating. In their subsequent research publication [13], heat flux of 325 W/cm² at a wall superheat of 7.3°C was obtained for a surface with porous microchannel fin tops using two step electrodeposition. From high speed images, they found that, bubbles nucleated on fin tops which enabled liquid re-entry from the microchannels to the pores.

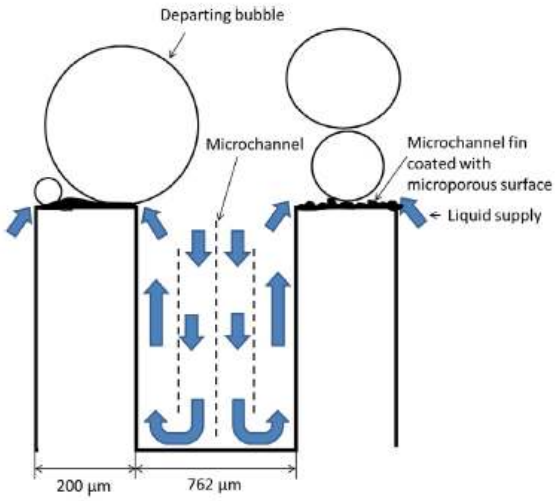

Figure 8: Micro convective flow through microchannel due to porous structure on fin tops

Webb[14] conducted a series of boiling experiments to study the effect of geometric parameters of porous coatings like particle size, pore size and coating thickness. The results revealed that a maximum HTC was obtained with a porous coating thickness of roughly four to six times the particle diameter. Additionally, it was suggested that the pore size has a more significant role compared to the overall porosity in enhancing the boiling heat transfer performance of porous surfaces.

Webiel [15] employed sintered copper wicked surfaces in evaporator sections of heat pipes and obtained heat fluxes greater than 500 W/cm² without the dry outs. They also stated that the cavities on the porous network play an important role by acting as nucleation sites. As the bubbles depart, the smaller nucleation sites underneath the departing bubbles become active and the rapid evolution of bubbles creates a large vapor column and turbulent convective flow, enhancing the heat transfer rate. Hanlon and Ma [16] fabricated a porous medium from a 100 mesh (149µm) 99.9% pure copper particles sintered at 840–900◦C for 12–45 min. They gradually decreased the thickness of the porous layer to study the effect

of thickness on the boiling performance. Based on their experimental work, they concluded that only the top surface of the wick plays an important role in heat transfer enhancement. Also, the heat transfer was improved by decreasing the particle size. They also observed that dry out heat flux depends significantly on the wick (layer) thickness.

Li, Wang et al.[17] developed various microstructures, nanostructures, and hybrid micro, nano structures on copper surfaces and discovered that the CHF for hybrid surfaces was about 15% more than that of the only nanowires and micro pillars. CHF of 250 W/cm^2 at wall superheat of 28°C was reached for combined micro-pillar and nanowire sample.

2.1.2 Heat transfer improvement – Effect of wettability and surface energy

The surface wettability is another key factor affecting CHF Surface with high wettability has been identified to enhance phase change heat transfer. Kandlikar [18] developed theoretical model to describe the hydrodynamic behavior of vapor liquid interface of a bubble leading to initiation of CHF. The wettability of a surface can be tuned by changing its surface morphology. Liquid wettability is the ability of a liquid to spread across the soild surface. Betz et al. [19] conducted a systematic study on combination of hydrophilic an hydrophobic surfaces. And revealed that the hydrophobic zones promote nucleation and the surface hydrophilicity helps in enhancing the CHF. The CHF value was increased by 65%, while the heat transfer coefficient was increased by 100% to the original value. Also, they found that substantial enhancement was observed with surfaces encompassing hydrophilic network with hydrophobic islands as shown in Fig 9. [19]

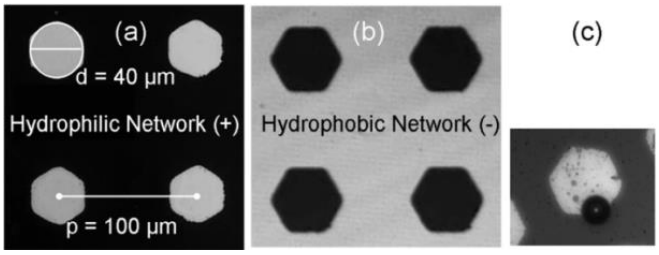

Figure 9: (a), (b) Micrographs of surfaces with hydrophilic (black) and hydrophobic (gray) zones; d (diameter of pattern) and p (pitch) (c) Nucleation of bubble

Hydrophilic networks prevent the formation of insulating vapor layer. Different networks were evaluated and it was found that the hydrophobic surface promotes the nucleation in the beginning, which results in boiling at low wall superheat, with increased heat flux the hydrophilic network promotes the higher heat flux by preventing the formation of insulation vapor layer.

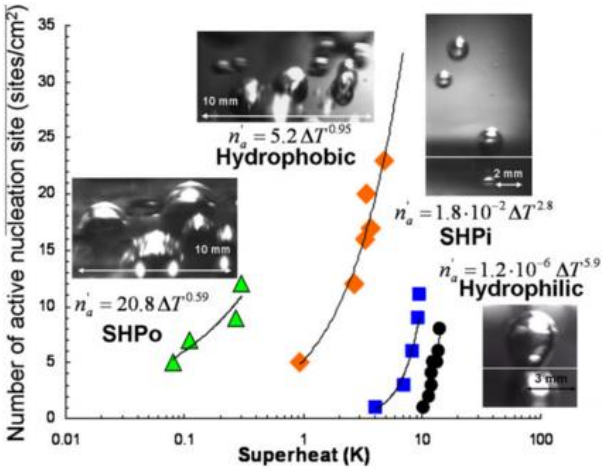

Figure 10: Measured density for active nucleation sites(white line as solid liquid interface) [19]

The bubbles in contact with the hydrophobic surface do not detach from the surface due to their higher curvature radius that increases with time. At higher heat fluxes, bubbles spread over the surface and coalesces resulting in a large vapor blanketed area.[20]

Hanley et al. [21] studied the individual effects of surface wettability, porosity and roughness on CHF and observed that the porous hydrophilic surfaces enhanced CHF by 50%-60% while porous hydrophobic surfaces reduced CHF by 97%. Rahman et al. [22] used bio-templated virus to generate micropillar wick structures and demonstrated that the wickability is the dominant factor dictating the CHF of structured surfaces. Through this technique, they demonstrated that the wicked volume flux underneath a growing bubble determined the increase in CHF. For the enhanced structures, a CHF of 257 W/cm² was achieved.

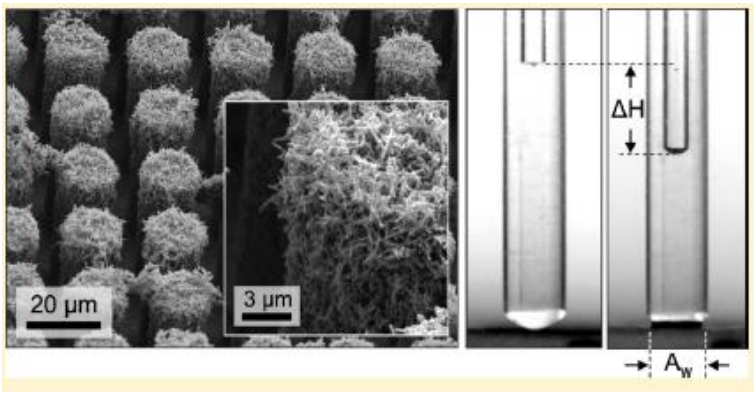

Figure 11: Role of wickability in enhancing the CHF [22]

2.1.3 Enhancement in heat transfer performance – Carbon derivatives

Carbon and carbon derivatives have shown promising enhancements in pool boiling applications. Berber et al. [23] used carbon nanofluid with homogeneously suspended Carbon Nanotubes (CNTs) that were coated on the surface after boiling Which led to the hypothesis that the enhancement in boiling was caused due to the coating of CNTs on the surface This prompted further investigations into the growth of CNT on boiling surfaces, exhibiting thermal conductivity values of up to 6600 W/m K at room temperature. They

also found that, once graphene layers are stacked in graphite, interlayer interaction quench the thermal conductivity of system by nearly 1 order of magnitude.

Novoselove et al. [24] successfully synthesized the graphene material with a high thermal conductivity of 5300 W/m K. Since then many researchers have employed various graphene and graphite structures to enhance the pool boiling performance.

Jaikumar et al.[25] performed the electrochemical deposition of copper with graphene using potentiostatic deposition of copper on platinum disc electrode followed by dip coating of graphene at various durations. 82% enhancement in HTC was obtained for the surface. Another study by Protich et al. [26] involved electrochemical deposition of copper in Graphene Quantum Dot bath. String like structure of composite was obtained which gave CHF of 216 W/cm² and HTC of 86 kW/m²°C. Improved performance was obtained due to higher thermal conductivity of graphene layers arising from the porous surface with increased surface area.

Park et al. [27] studied the effects of Graphene Oxide (GO) -based nanofluids boiling over a thin-wire heater in horizontal and vertical orientations. In these configurations, they reported enhancements of over 40-200% in CHF. These enhancements were attributed to the complex nature of self-assembling characteristics of graphene nanoparticles on the boiling surface. The self-assembly of graphene-layers results in a change in surface morphology which directly correlates with the increase in CHF. Method of dip coating copper chips in a solution consisting graphene and graphene oxide was investigated by Jaikumar et al.[28] Different characterization techniques were used to confirm the presence of graphene and graphene oxide. CHF of 182 W/cm² was obtained and the roughness was observed to be an influencing factor for improvement. Ahn et al. [29] sprayed Reduced

Graphene Oxide (RGO) flakes on copper substrates. The RGO colloid was synthesized by chemical reduction of hydrazine from graphene oxide. They identified that increased wettability and increase in percentage of GO led to significantly enhanced boiling characteristics. Ahn et al. [30] postulated that thermal conductivity of RGO played a significant role in increasing the CHF while, the wall temperature did not increase rapidly. In another study, Kim et al. [31] reported high hydrophobic wetting as a consequence of layer build up on the substrates. The large thermal conductivity of GO layer inhibited the formation of local hotspots and prevented the formation of dry-out regions and which in turn improved the CHF. Mejia et al. [32] used electrochemical deposition method for deposition of graphite/graphene composites on copper substrates. Different electrochemical baths of water, and ethanol were used for the deposition process. They achieved CHF of 269 W/cm² at wall superheat of 23°C for the deposited surfaces. Raj et al. [33] have shown that the advancing contact angles are a true representation of wettability in graphene coatings, while the receding contact angles were dictated by the defects on the surface which results in contact angle hysteresis. They also found that advancing contact angle measurements were independent of layers of graphene.

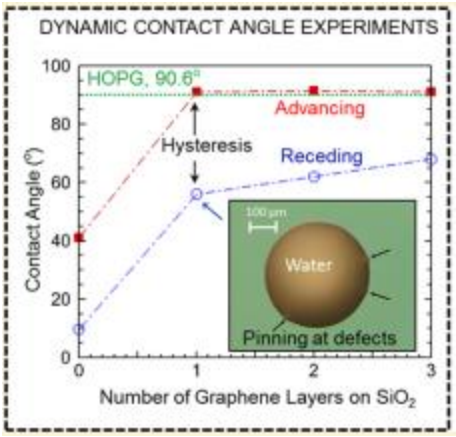

Figure 12: Advancing and receding contact angles with increase in graphene layers [33]

2.2 Scope of work

As noted from the literature review, graphene and graphene oxide have a huge impact on enhancing the CHF due to very high thermal conductivity of graphene. Additionally, it also improves the heat transfer rate by reducing the wall superheat. This research work focuses on enhancing the pool boiling heat transfer performance of a plain copper chip by combining the electrodeposition of copper and graphene oxide with distilled water as a working fluid at atmospheric pressure. Electrodeposition of combination of metal and non-metal can be the key factor to drastically enhance the CHF by reducing the wall superheat temperatures simultaneously.

Electrodeposited and sintered surfaces have significant effects on morphologies and wettability due to continuous boiling tests. The performance over a period of time of the enhanced test surfaces has not been reported, and this work on investigation of the

longevity of the electrodeposited tests surfaces and its effect on the pool boiling performance fills the gap in the pool boiling studies. The work also highlights the role of graphene in enhancement in aging. To improve the bond strength and the adhesion of electrodeposited test surfaces, new multi-step electrodeposition technique is employed to improve the aging performance of the electrodeposited chips.

Chapter 3

This Chapter focuses on the electrodeposition technique used in this study to deposit copper and graphene on test copper surfaces and their pool boiling performance All the pool boiling tests are performed at atmospheric pressure and distilled water is used for the tests.

3.1 Experimental setup

3.1.1 Pool boiling setup

A schematic of the experimental setup used for the pool boiling tests of the test chips is shown in Figure 13. The test setup included a water bath, an instrumented test chip, and a heater. The test chip was placed in the ceramic chip holder with slots to insert the thermocouples. Only 10 mm x 10 mm area of the test chip surface was exposed to the boiling and remaining area was covered with Kapton® tape which acts as an insulation. Above the test chip, a quartz glass water bath, rectangular in cross section, with dimensions 14 mm x 14 mm x 38 mm was placed. To seal the contacting surfaces at the bottom and the top, a rubber gasket was used.

Two stainless steel socket head cap screws were used to hold the middle garolite plate and the top aluminum plate. In the top aluminum plate, an auxiliary cartridge type heater (60-VDC, 200W) of circular cross section was fitted along with a small circular hole to insert the saturation thermocouple probe.

Four cartridge type heaters of 120-VDC, 200W capacity were inserted into a copper heater block which was then placed on the ceramic block below the test chip. The heater block fits snugly into the groove on the bottom of ceramic chip holder. Grafoil sheet was placed

above the heater to minimize the air gap between chip and the heater. Aluminum block is placed below the ceramic block, which is supported by four compression springs to establish the correct contact between the heater block and the test chip. This also ensured only 1-D steady state conduction from heat source to the test chip.[34]

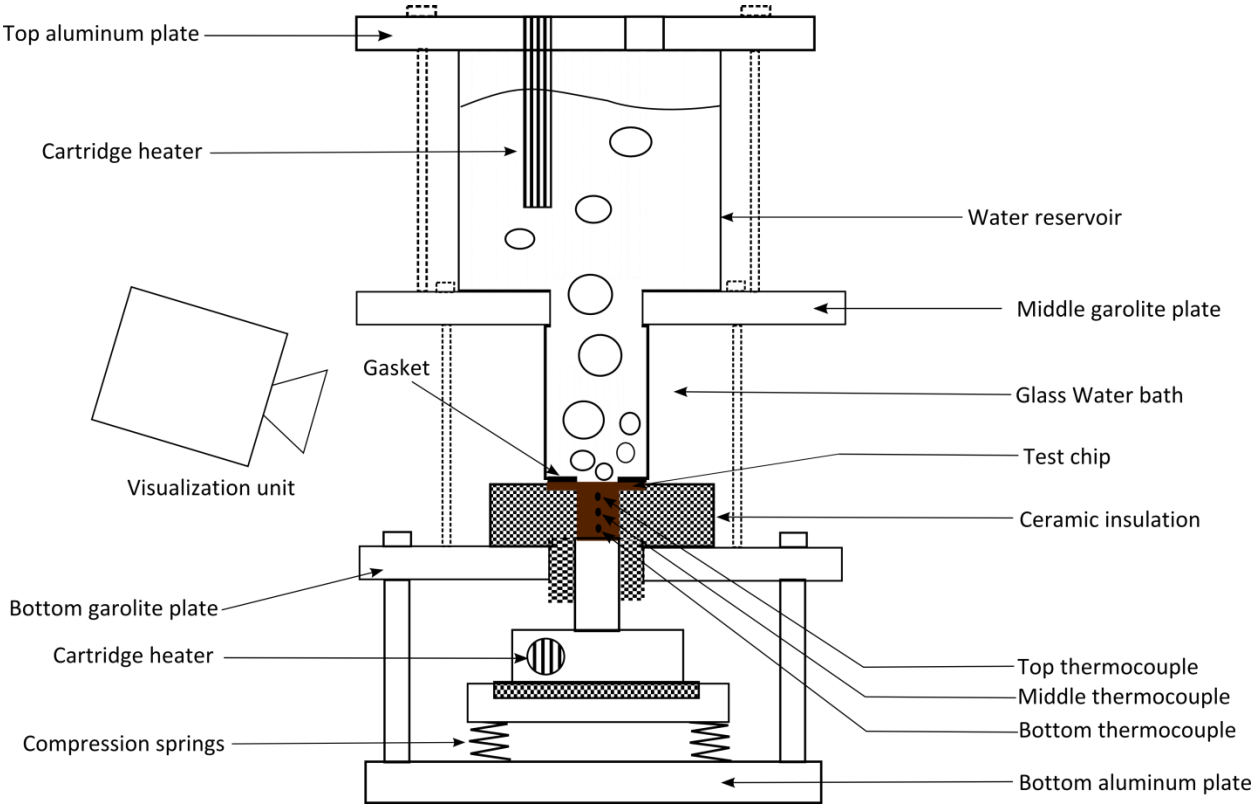

Figure 13: Pool boiling setup[34]

3.1.2 Test section

Plain test chips of made of copper alloy 101 were used in this study. Test chips consisted of a 17 mm x 17 mm x 9 mm surface with a 9-mm deep rectangular base to accommodate the thermocouples used for heat flux estimation. The thermocouple holes were drilled to reach the center of the rectangular base. As shown in Figure 14, the distance between the two successive holes on a rectangular base is 3 mm (Δx) while the distance between the

hole near the chip surface and the top of the chip is 1.5 mm. (x_1). To read the three temperatures, T1, T2, T3, thermocouples were inserted into the holes.

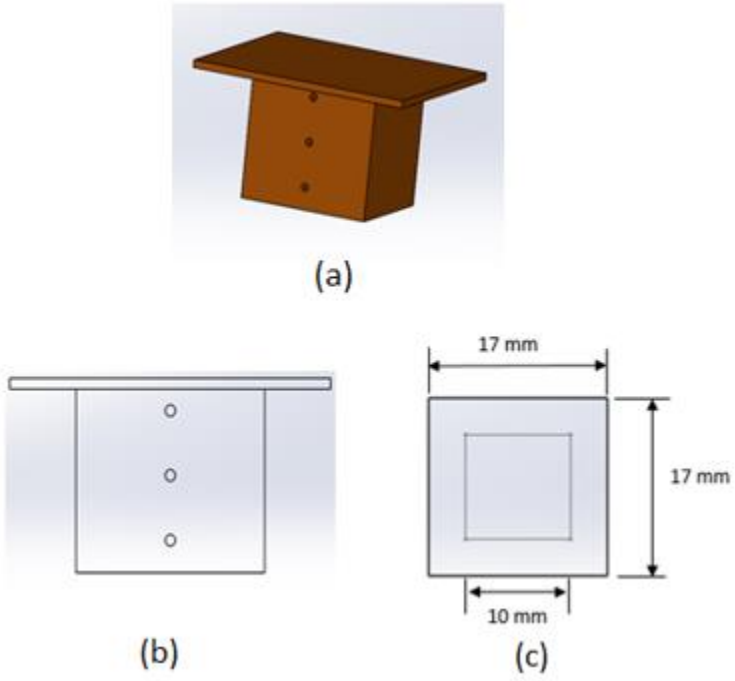

Figure 14: Plain copper chip (a) 3D view, (b) Front view, (c) Top view

3.1.3 Electrodeposition technique

Electrodeposition is one of the techniques by which porosity can be controlled by controlling the current density and time required for the deposition. In the setup, test section i.e. copper chip is cathode while copper block is used as anode. Princeton Applied Research VersaSTAT 3 and Gamry Instruments Series 300 is used for the deposition. Both cathode and anode are inserted vertically in the electrolyte bath which contains the $CuSO_4$ salts and distilled water. As shown in Figure 15, when direct current is supplied from the VersaSTAT 3, anode loses its electrons and cathode i.e. test section gains the electrons. The current in the solution always flows from anode to the cathode. Thus, when current is supplied, positive ions of Cu^{2+} are formed at the anode which travel towards the cathode.

Meanwhile, the sulphate ions (SO_4^{2-}) are discharged from the electrolyte solution and travel to anode, which completes the electric circuit.

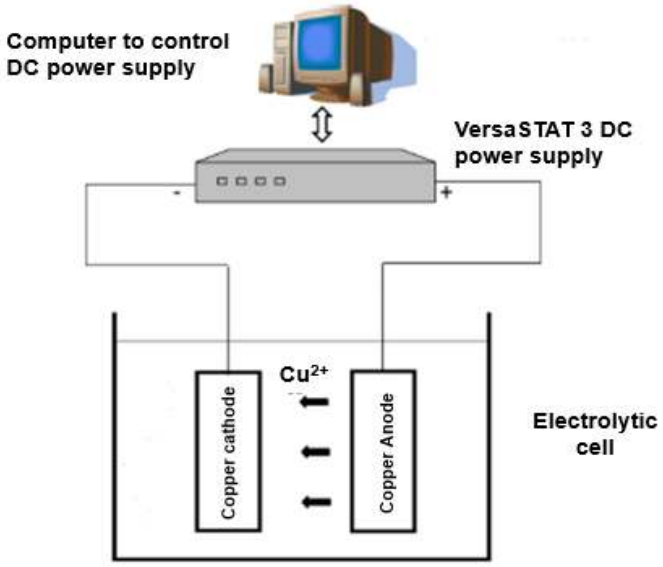

Figure 15: Electrodeposition technique

The electrochemical deposition process is accomplished through two reactions. At cathode, electrons are supplied. Since the deposition occurs at cathode, cathode undergoes reduction. Thus, reaction at cathode is given by:

$$C^{d+} + ne^- \rightarrow C \quad (4)$$

At anode, electrons are migrated from the surface towards the cathode, causing oxidation at anode Hence, reaction at anode is given by:

$$C \rightarrow C^{d+} + ne^- \quad (5)$$

The electrons freed from anode to form the metal cations travel to cathode and get deposited at cathode. This forms the coating at the cathode. The coating on cathode is of the same material as that of the anode. In the electrochemical reaction, cathode undergoes reduction while anode undergoes oxidation. According to Faraday's law of electrolysis [39]

[40], the amount of the deposited material is proportional to the duration of the electrodeposition and the time of the deposition.

The process of electrodeposition can be done in two ways: (i) supplying the constant current throughout the deposition, and (ii) holding the constant potential throughout the deposition. These methods are called as Galvanostatic and potentiostatic methods of deposition respectively. In the current study, all the depositions are performed using Galvanostatic method, i.e. the constant current is supplied for the fixed duration and the voltage is varied accordingly.

3.1.4 Electrochemistry setup

Plain copper chip is initially cleaned with Isopropyl Alcohol (IPA) and distilled water to remove any impurities if present on the test chip. Test chip with the central 10mm × 10mm area is then marked and the area outside this region is covered with electrical insulation tape. This is done to avoid any deposition occurring on the region outside the central test area.

For the electrodeposition of copper on the plain chip, 0.8M $CuSO_4$ solution (5.85 gm) and 1.5M conc. H_2SO_4 solution (3.14 mL) is mixed with 40 mL of distilled water.[41] Since the chemical reaction of $CuSO_4$ and H_2SO_4 is exothermic, water is added in two intervals, 20 mL before adding H_2SO_4 and 20 mL after adding H_2SO_4. Sonicator is then used to make the solution homogeneous and to dissolve the copper sulfate powder completely in the solution.

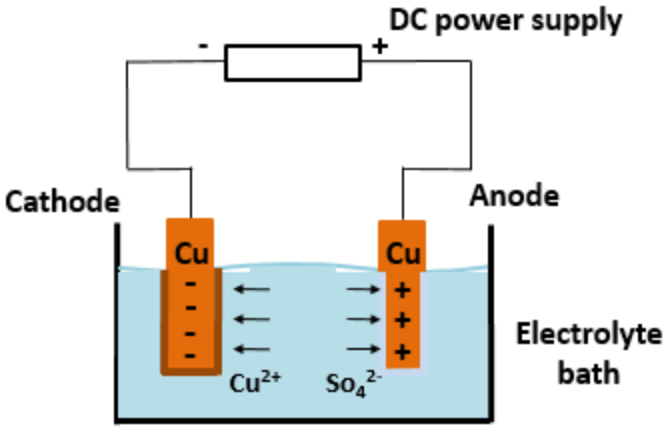

Figure 16: Electrodeposition setup

Figure 16 shows the setup used for the electrodeposition technique. Galvanostatic method is used for the deposition. Deposition is conducted in a two-step process in which the first step is the deposition of copper while the second step is enhancing the bonding of deposited copper with the base material. For the step 1, current density of 400 mA is applied for 15 seconds, while for the second step; a current of 40 mA is applied for 2500 seconds. [13]

From the literature study, it is found that apart from the deposition technique, type of coating material also plays a vital role in the porosity and the morphology of the electrodeposited surface. For the preliminary work, a combination of metal and nonmetal (Graphene Oxide) in an electrolyte solution is used for the deposition. Non-metal solution of graphene is added in the electrolyte solution at various percentages- of 0.5, 1, 1.5, 2. Table 1 shows the test matrix for the plain copper chips. Total four test chips of copper and graphene oxide are prepared, while one controlled chip of copper deposition is prepared for the comparison.

Table 1: Test matrix for plain chips

Test chip #	Composition (Electrodeposition)
Chip 1 (Cu on Cu)	Cu on Cu
Chip 2 (GS-1)	Cu + 0.5% GO
Chip 3 (GS-2)	Cu + 1.0% GO
Chip 4 (GS-3)	Cu + 1.5% GO
Chip 5 (GS-4)	Cu + 2.5% GO

3.2 Data acquisition

To record the temperatures given by the thermocouples, a National Instruments cDaq-9172 data acquisition system with NI-9211 temperature module was used. Overall four thermocouples were used, out of which three were inserted into the slots provided in the test section for heat flux measurement and surface temperature determination, while the fourth was inserted from the top of aluminum block to measure the saturated temperature. A LabVIEW VR virtual instrument is displayed and the surface temperature and heat flux was calculated. Apart from that, Lab View also shows the graphical variation of temperature with respect to time of each thermocouple. This is useful for determining the critical heat flux spikes.

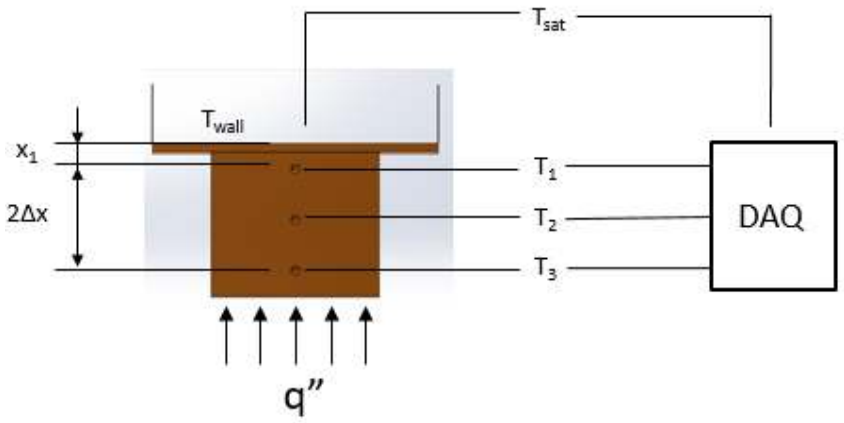

Figure 17: Schematic of data acquisition and heater assembly

Heat flux is calculated using steady state 1D conduction equation

$$q'' = -k_{Cu}\frac{dT}{dx} \tag{6}$$

Where, the temperature gradient dT/dx was calculated using the three point backward Taylor's series approximation

$$\frac{dT}{dx} = \frac{3T_1 - 4T_2 + T_3}{2\Delta x} \tag{7}$$

The boiling surface temperature was obtained by using eq. 1 and 2, and is given by

$$T_{wall} = T_1 - q''\left(\frac{x_1}{k_{Cu}}\right) \tag{8}$$

3.3 Uncertainty analysis

During the experiment, a certain amount of error occurs in measuring the values. The two main errors are precision error and bias error. Bias errors are the difference between expected measurement value and the true measurement value. So, bias errors are the errors due to calibration while precision errors are due to the sensitivity of the testing instruments. A complete uncertainty analysis was performed similar to Patil and Kandlikar[40] and Mejia and Kandlikar.[41] Errors due to precision and bias uncertainty are expressed as:

$$U_y = \sqrt{B_y^2 + P_y^2} \tag{9}$$

Where, U_y is the uncertainty of parameter y. P_y is the precision error and B_y is the bias error. Table 2 shows the parameters associated with precision errors and the source of these errors, which includes thermocouple temperatures, thermal conductivity of copper and the machining of test chip. The thermocouples are calibrated and its precision error was computed statistically to be ± 0.1 °C.

Table 2: Uncertainty parameters and sources of errors

Parameter	Value	Units	Precision error (U_P)	% uncertainty
T_{TOP}	Varies	°C	0.0763	Varies
T_{MIDDLE}	Varies	°C	0.0756	Varies
T_{BOTTOM}	Varies	°C	0.0791	Varies
k_{Cu}	391	W/m°C	9	2
Δx	3.00E-03	m	1.00E-04	3
Δx_1	1.50E-03	m	1.00E-04	6

$$U_p = \sqrt{\sum_{i=1}^{n} \left(\frac{\partial p}{\partial a} * u_{ai}\right)^2} \tag{10}$$

Where U_p is the uncertainty in the parameter p, and u_{ai} is the uncertainty of measured parameter a_i. The uncertainty in the heat flux and heat transfer coefficient can thus be expressed by the equations 11 and 12 respectively.

$$\frac{U_{q"}}{q"} = \sqrt{\left[\left(\frac{U_k}{k}\right)^2 + \left(\frac{3U_{T_1} * k_{Cu}}{\Delta x * q"}\right)^2 + \left(\frac{4U_{T_2} * k_{Cu}}{\Delta x * q"}\right)^2 + \left(\frac{U_{T_3} * k_{Cu}}{\Delta x * q"}\right)^2 + \left(\frac{U_{\Delta x}}{\Delta x}\right)^2\right]} \tag{11}$$

$$\frac{U_h}{h} = \sqrt{\frac{U_{q"}^2}{q"^2} + \frac{U_{T_w}^2}{\Delta T_{sat}^2} + \frac{U_{T_{sat}}^2}{\Delta T_{sat}^2}} \tag{12}$$

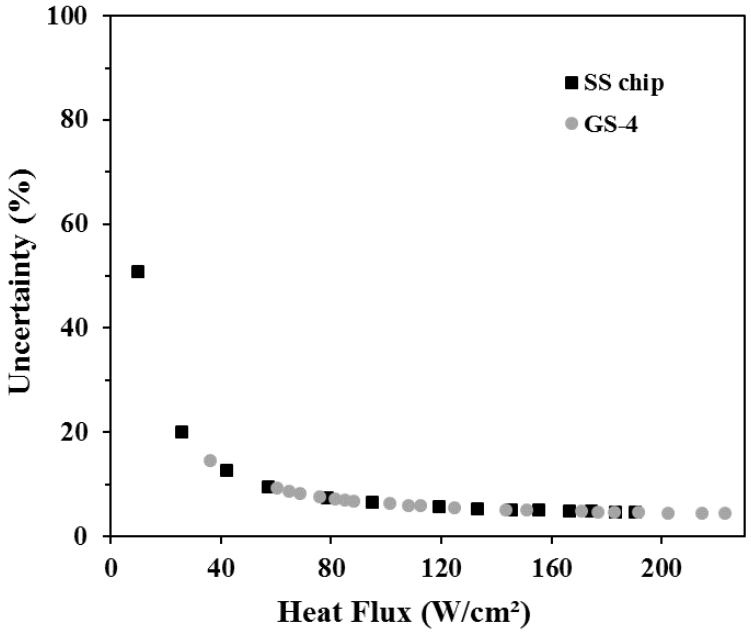

Figure 18: Uncertainty in heat flux for Six Step (SS) Cu on Cu electrodeposited chip and GS-4 (2.5% GO-Cu) electrodeposited chip

It was observed that uncertainty decreases with increase in heat flux. The main aim of this study is to have the uncertainty below 5% at higher heat fluxes and at CHF. Similar calculations were done to find the uncertainty in HTC (h). The uncertainty was found to be below 5% in the same region.

3.4 Characterization of surface

3.4.1 Scanning Electron Microscope (SEM)

The distinct morphological structures of copper and graphene oxide for the aging studies analysed using a JSM-6400V and TESCAN Field Emission Mira III scanning electron microscope (SEM), at an accelerating voltage of 15 kV. The energy dispersive X-ray spectroscopy (EDS) measurements were done on Bruker Quantax EDS with XFLASH

5010 detector attached to a field emission scanning electron microscope MIRA II LMH to the presence of various elements on the sample. [43]

The unique morphology of the samples of GO and copper are obtained through the electrodeposition process. As shown in Fig.19, "Bitter gourd" like structure is formed from the combination of copper and graphene oxide deposition. EDS mapping as shown in Fig.19 confirms the presence of carbon, oxygen and copper on this Bitter gourd structure. Detailed explanation of SEM images is given in Chapter 4.

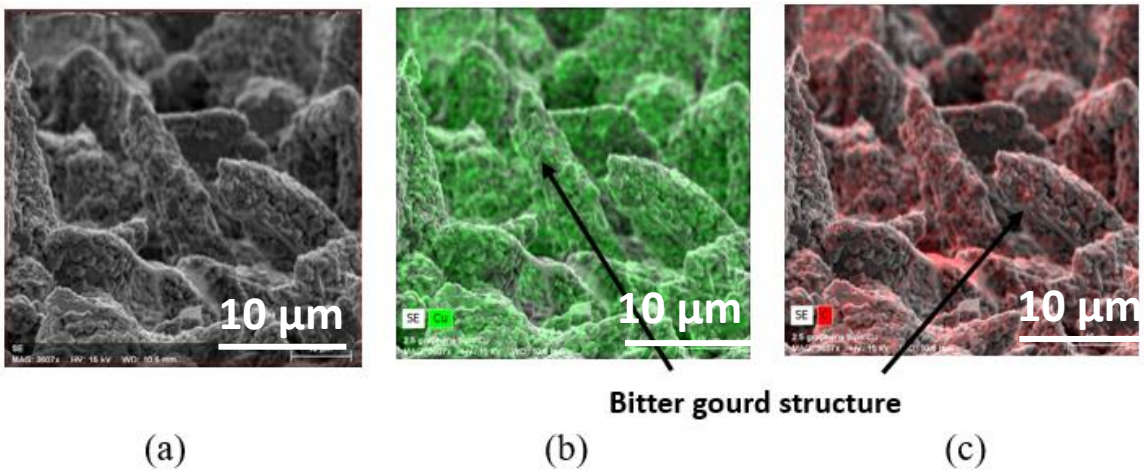

Figure 19: SEM images of the electrodeposited surface using Galvanostatic method. (a) Bitter gourd copper structures at 3.6 kX, 70° tilt, (b) Energy dispersive X-ray spectroscopy (EDS) showing copper mapping confirming Bitter gourd structures were made of copper, (c) Energy dispersive X-ray spectroscopy (EDS) showing the traces of carbon on Bitter gourd structure

3.4.2 Contact angle study

Static, advancing and receding contact angles were measured on both the surfaces. Contact angle measurements were done using VCA Optima Goniometer Instrument. Measurements of the contact angles were recorded on the VCA software which showed the real-time visualization of the droplet. For calculating the contact angle, five points were used to trace

the shape of the drop and then left side and the right-side contact angle of the droplet was displayed.

Static contact angle was measured by dropping the specific quantity (2 µL) of the droplet of water on the surface and stabilizing it for 5 seconds. For measuring the advancing contact angle, syringe was used to drop a certain volume of water (4 µL) on the surface. The angle was measured when the size of the droplet was increased and when the droplet of water slide outward on surface compared to its previous position. The maximum value of the contact angle was recorded as the advancing contact angle. Similarly, for measuring the receding contact angle, water from the chip surface was drawn into the syringe, and the point at which the water droplet changed its shape from convex to concave, the contact angle was measured. This was recorded as the receding contact angle. The difference between advancing and receding contact angle is called as the hysteresis of contact angle.

Table 3: Contact angles of test chips (refer table #1)

Test chip	Contact angle (°)			
	Static	Advancing	Receding	Hysteresis
Cu on Cu	53	67	18.4	48.6
GS-1	109.3	58.1	22.4	35.6
GS-2	87.5	36.4	14.3	22.1
GS-3	54.5	33.6	13	20.6
GS-4	48.5	42.6	13.5	29.1

3.4.3 Wicking Rate

Wicking is the property of micro porous structure which measured the volume of droplet wicked or absorbed in a particular period. For measuring the wicking rate, fixed volume of water (2 µL) was dropped on the chip surface and dynamic contact angle data of the droplet was taken. A sessile drop method [44] was used to measure the wicking rate. A pendant water droplet was slowly brought contact to the electrodeposited test surfaces. Using high speed camera, rate of change of volume of droplet was measured on a software on frame basis. The wicking rates of each surface was measured by visualizing the dynamic spreading behavior of a drop placed on these surfaces. The volumetric change in a liquid droplet of a fixed volume was captured for a duration of ~75 s using a VCA Optima goniometer.

3.5 Results

3.5.1 Comparison of CHF and HTC:

Figure 20 shows the pool boiling curves obtained with the GS1-4. The GO composition in these samples varied between 0.5-2.5 percent by volume. The deposition was carried out in a carefully designed electrochemical cell using a Galvanostatic method as discussed previously. GS-1, GS-2 and GS-3 reached a CHF of 135 W/cm², 169 W/cm² and 194 W/cm², respectively. A CHF of 220 W/cm² was obtained with GS-4 corresponding to the sample with the maximum GO composition of 2.5 percent. To the best of the authors' knowledge, this is currently the highest reported CHF with graphene-based coatings. The

test surfaces in this data set resulted in an increase in CHF with a simultaneous reduction in wall superheat.

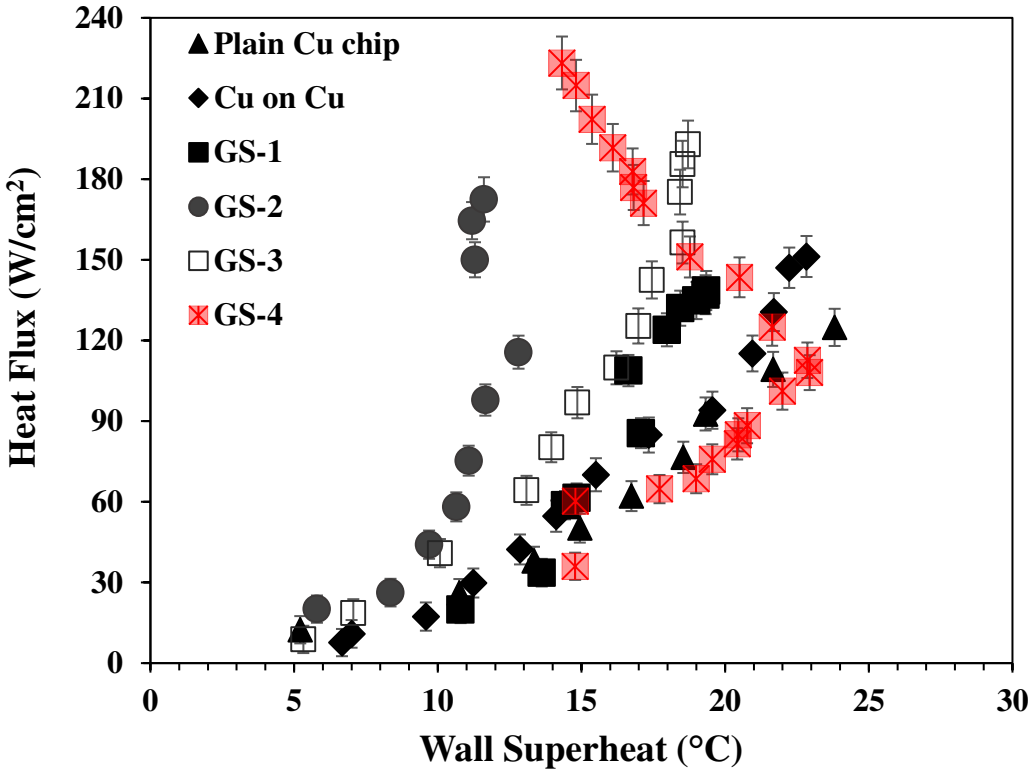

Figure 20: Comparison of pool boiling performance

Figure 21 shows the HTC plots obtained for the surfaces prepared using the Galvanostatic process. In these samples, a significant increase in HTC in addition to CHF increase was observed. A maximum HTC of 72 kW/m² °C, 155 kW/m² °C, 103 kW/m² °C and 155 kW/m² °C at CHF was achieved with GS-1, GS-2, GS-3 and GS-4, respectively. The trend in the investigated surfaces suggest that the CHF increased with an increase in the GO concentration.

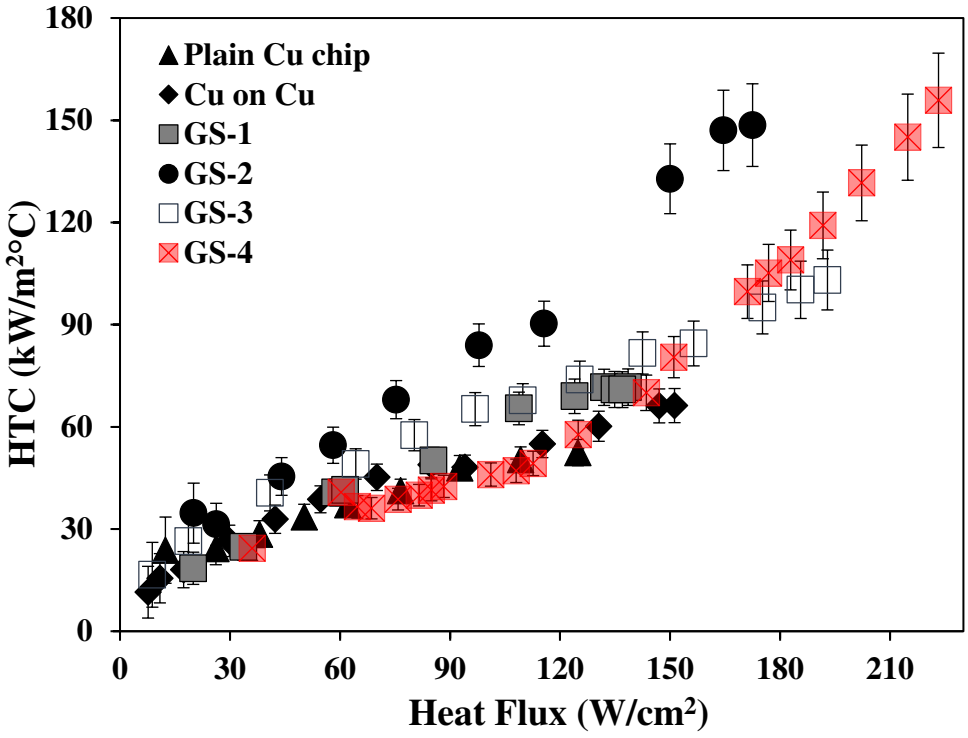

Figure 21: Comparison of heat transfer performance

3.5.2 Effect of % increase of Graphene Oxide (GO)

The percentage of graphene oxide was increased by volume in an electrolyte solution. This percentage was increased from 0.5, 1, 1.5 up to 2.5% GO in an electrolyte solution containing distilled water, copper sulfate and sulphuric acid. From the plot 22, it is seen that the heat flux increases with an increase in the percentage of GO in electrolyte solution.

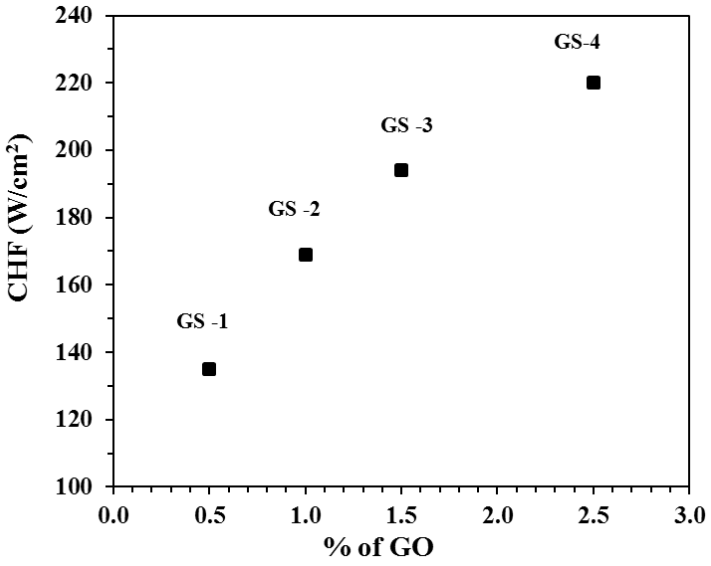

Figure 22: Effect of % increase of Graphene Oxide (GO)

3.5.3 Effect of wicking

The wicking rates play a significant role in enhancing the CHF. Rahman et al. [27] demonstrated this effect by introducing a dimensionless parameter, wicking number (*Wi*), which directly correlated to the increase in CHF using bio-templated structures.

Figure 21 shows the variation of CHF with the (1 + *Wi)* for the surfaces investigated here. The wicking number is calculated using (13) as described by Rahman et al. [27].

$$W_i = \frac{V''_0 * \rho_l}{\sqrt{\rho}_v * [\sigma * g * (\rho_l - \rho_v)]^{1/4}} \quad (13)$$

Where,

Wi is wicking number, V_0'' is the wicking rate (m/s), ρ_l and ρ_v are the liquid and vapor densities (kg/m³), g is the acceleration due to gravity (m/s²), and σ is the surface tension (N/m). The wicked volume (mm³/s) is estimated as the droplet volume change over time

using a VCA Optima goniometer. The wicking rate (mm/s) is calculated by normalizing the wicked volume over the droplet impingement area. [8]

It is noted from Figure 23, that the CHF increases with an increase in the wicking number. The application of the CHF model proposed by Rahman et al. [27] predicts a CHF of less than 150 W/cm^2 which is less than the experimental values obtained in this data set. Therefore, we recognize that additional mechanisms were further responsible for the enhancement.

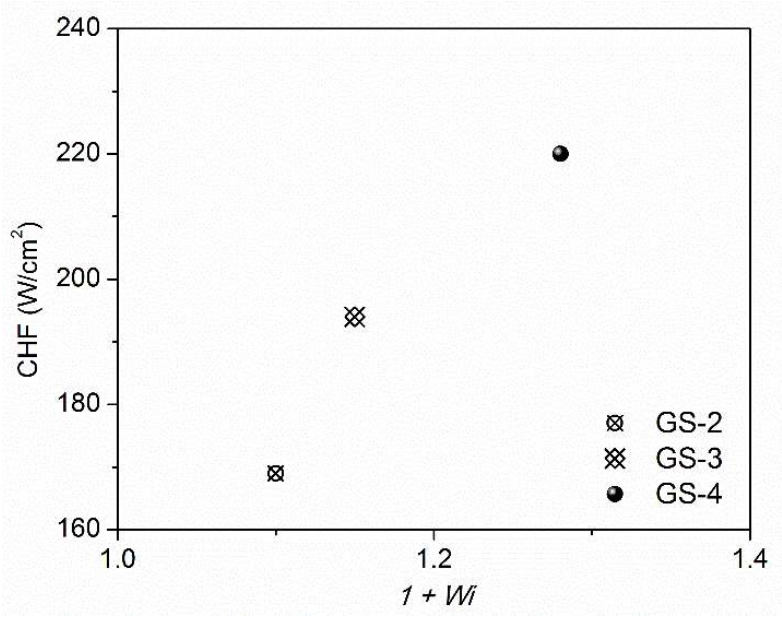

Figure 23: Effect of wicking on GO-Cu electrodeposited chips (refer table 1)

Additional nucleation sites and microlayer partitioning mechanisms

In the samples investigated here (GS-1through GS-4), the HTC is significantly increased due to the low wall superheats at relatively higher heat fluxes. GS-2 and GS-4, in addition to wicking, have increased nucleation sites that are activated under suitable superheat

conditions and contribute towards decreasing the wall superheat. The mechanism for such a trend is attributed to the range of cavity sizes available for nucleation as discussed previously. The nucleation activity is further promoted by the enhanced evaporation through microlayer partitioning mechanisms. Maroo et al. proposed this mechanism by fabricating silicon ridges in the nano/microscale [45]. Similarly, Jaikumar et al. [27] have shown the microlayer partitioning on graphene surfaces contributed towards increasing the growth rates and bubble frequency. [43]

The enhancements in CHF and HTC are due to the relative effects of wicking and additional nucleation sites. The microscale morphology of the samples play a critical role in enhancing wicking and promoting nucleation. The features promote wicking through the copper-dendrites and nucleation through the GO sheets. The nucleation activity increases due to microlayer partitioning mechanisms, as demonstrated by Jaikumar and Kandlikar [27] and Zou and Maroo [45]. The microlayer partitioning increases bubble growth rates and frequency. This arrangement results in an increase in both CHF and HTC characteristics demonstrated here. The effect of additional nucleation sites and wicking are the main contributing mechanisms for enhancing the CHF and HTC of GS-4.

Chapter 4

From Chapter 3 it is seen that electrodeposition of combination of copper and graphene oxide helps to enhance the heat transfer performance drastically by keeping the wall superheat low. 220 W/cm² heat flux is obtained for GS-4 (2.5% graphene) chip, which is the highest heat flux that has ever been obtained for any graphene based coating on plain copper chip with a 14°C wall superheat.

As mentioned earlier, this section of the thesis aims to fill the gap in the literature on the prolonged stability of the enhanced surfaces by focusing on the longevity and the aging studies of the electrodeposited chips. The extensive studies conducted in this thesis demonstrated the peeling of the coating on the controlled chip (copper on copper) whereas, the graphene coating sustained despite the pool boiling tests.

For the ageing studies, the best performing chips with 2.5 % graphene oxide coatings from the previous chapter were considered along with the control plain copper chip.

4.1 Development of the test method

This chapter focuses on enhancements in prolonged stability due to electrodeposition of combination of graphene oxide and copper.

The pool boiling setup mentioned in Chapter 2 was used for all the tests. A DC power source was used to supply the power to main heater. The voltage was increased and then kept constant till the saturation of the fluid was reached. All the four temperatures, i.e. T_1,

T_2, T_3 and the bulk fluid temperature were measured using K type thermocouples and displayed in LabVIEW. (Refer Fig. 17)

When the steady state was reached, data was logged for 10 seconds with 4 data points per second. The voltage of the DC power source was increased by 5 Volts and data was recorded after reaching the steady state. The steady state corresponds to ±0.1°C change in the readings of chip temperatures for 10 minutes. For the part 1, to age the chip, same chip was tested again and again for 20 times. Each time the heat flux was raised up to 80 W/cm^2, and chip was kept running at the same heat flux for 15 minutes, and then was reduced back to zero by reducing the voltage by 5 Volts and tracing the path backwards. The similar test was repeated for 20 times. Total 85 hours of pool boiling test was performed. After that, the same chip was tested till it reaches the maximum heat flux (CHF). The CHF performance of the fresh chip and the aged chip was then compared.

Similarly, the same numbers of tests were performed on plain copper chip and the CHF was compared. However, due to heavy oxidation of the plain copper chip after 20 runs, it was not tested for the CHF. Table below shows the test matrix for the part 1 of the aging study.

Table 4: Test matrix for aging study of GalvanoStatic (GS-4) and Plain copper chip

Chip	No. of runs
Plain Cu	20
2.5% GO-Cu Electrodeposited chip (GS-4)	20

4.2 Characterization

4.2.1 Contact angle study

Similar to Chapter 3, static, advancing and receding contact angles for both the surfaces were measured. Contact angle measurements were done using VCA Optima Goniometer Instrument.

Contact angles were measured before the test, i.e. on the fresh samples and to observe the change in morphology, contact angles were measured again after 20 repetitive pool boiling tests. Table 5 shows the contact angle data for plain copper chip and 2.5% GO-Cu electrodeposited chip.

Table 5: Contact angles of fresh and aged plain copper and 2.5% GO-Cu electrodeposited chips

Test Chip	**Before the test (fresh chip)**				**After 20 runs (aged chip)**			
Plain Cu chip (PC)	Static	Advancing	Receding	Hysteresis	Static	Advancing	Receding	Hysteresis
	82.5	89.5	24.6	64.9	68.5	81.5	18.3	63.2
2.5% GO-Cu electrodeposited chip (GS – 4)	48.5	42.6	13.5	29.1	140	145	38.6	106.4

4.2.2 Wicking Rate

Wicking rate for 2.5% GO-Cu electrodeposited (GS-4) chip was measured using the similar procedure as explained in Chapter 3. Wicking rate of the chip was taken before and after the aging of the sample. Figure 24 shows the change of contact angle over the time. LA represents the Left Angle and RA represents the Right Angle of the droplet. In the figure, the gray line plot shows the change in contact angle of GS-4 chip before the pool boiling test, while the black line graph shows the change in contact angle of the GS-4 aged chip.

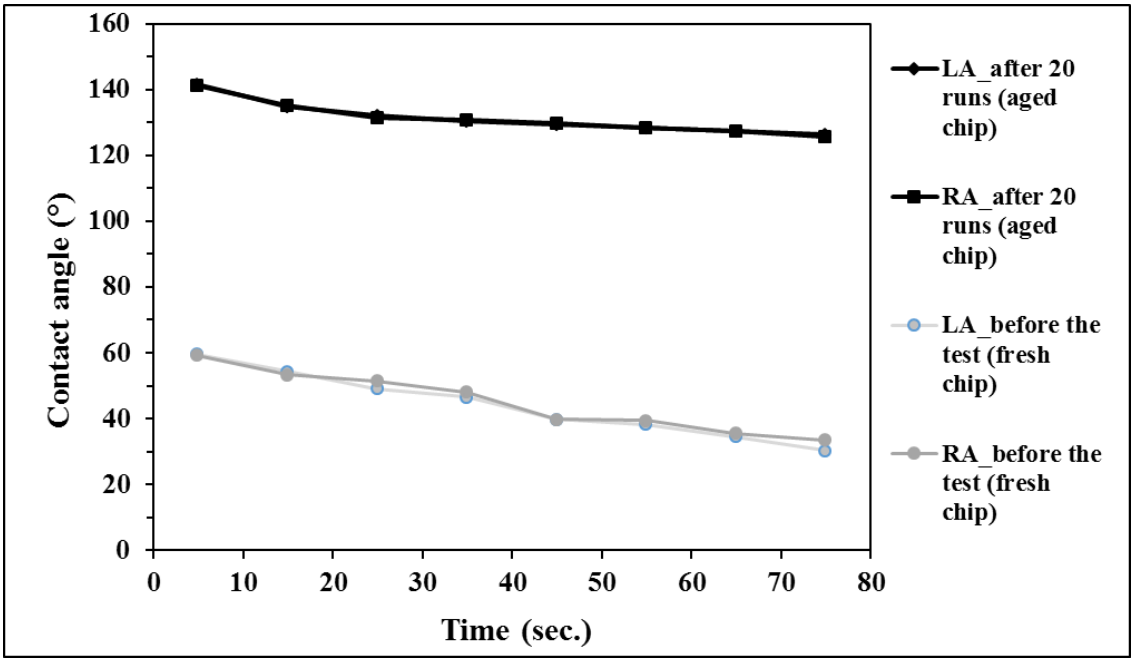

Figure 24: Change in contact angle over time of left and right side of the droplet (LA and RA respectively) for fresh and aged 2.5% GO-Cu electrodeposited chip (GS-4)

4.2.3 Scanning Electron Microscope (SEM)

A Scanning Electron Microscope (SEM) is used for analysis of microstructural characteristics of a surface by producing images of the sample by scanning the sample surface with a focused beam of electrons. [46] Since SEM uses electrons instead of lenses to capture the image, hence, the degree of magnification can be controlled.

The distinct morphological structures of copper and graphene oxide for the aging studies analysed using a JSM-6400V and TESCAN Field Emission Mira III scanning electron microscope (SEM), at an accelerating voltage of 15 kV. The energy dispersive X-ray spectroscopy (EDS) measurements were done on Bruker Quantax EDS with XFLASH 5010 detector attached to a field emission scanning electron microscope MIRA II LMH to the presence of various elements on the sample. The "bitter gourd" like structures were formed as a result of graphene coated on the dendritic copper structures. The presence of both copper and carbon elements were confirmed by the as shown in Fig. 25 b and c.

Figure 25 represents the SEM analysis of 2.5% GO-Cu electrodeposited chip before performing any pool boiling test. Fig.25 (a) shows the image of the surface at magnification of 3.6kX and at 70° tilt. The samples were also imaged by tilting the stage to gain an insight on the thickness, the height and additional features of the observed structures. From the tilted images, the thickness of the Bitter gourd structure was found to be around 6-8µm and height of the structure is 7-10µm. Despite of 20 repetitive tests, the morphology of the surface did not change much.

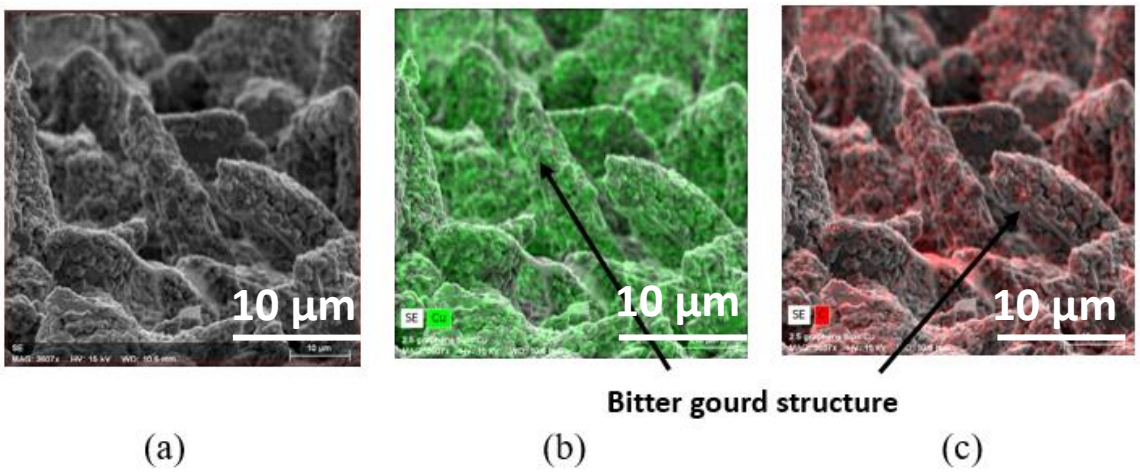

Figure 25: SEM images of the electrodeposited surface using Galvanostatic method. (a) Bitter gourd copper structures at 3.6 kX, 70° tilt, (b) Energy dispersive X-ray spectroscopy (EDS) showing copper mapping confirming Bitter gourd structures were made of copper, (c) Energy dispersive X-ray spectroscopy (EDS) showing the traces of carbon on Bitter gourd structure

After continuous 20 cycles of pool boiling, the bitter gourd morphology underwent subtle changes and demonstrated more succulent plants like structures with well-defined grains on the base dendrites. Figure 26 shows the comparison of morphology of the test chip before the test and after 20 pool boiling tests. It was observed that the structure became less dense and the thickness of the Bitter gourd structure was reduced from 8µm to 5µm after 20 repetitive pool boiling tests. Figure 26 (a) and (b) show EDS mapping of the images before and after the 20 tests respectively. To find the thickness and height of the structure, all the images were captured at 70° tilt angle. Image 26(a) and is at 3.6 kX magnification while image 26 (b)is at 2 kX magnification. The thickness and height of the structure is decreased by ~2 µm as compared to that of before boiling. But despite of continuous pool boiling tests, the structure in general has remained the same. EDS mapping confirms the presence of carbon and copper on the test chip even after 20 repetitive tests.

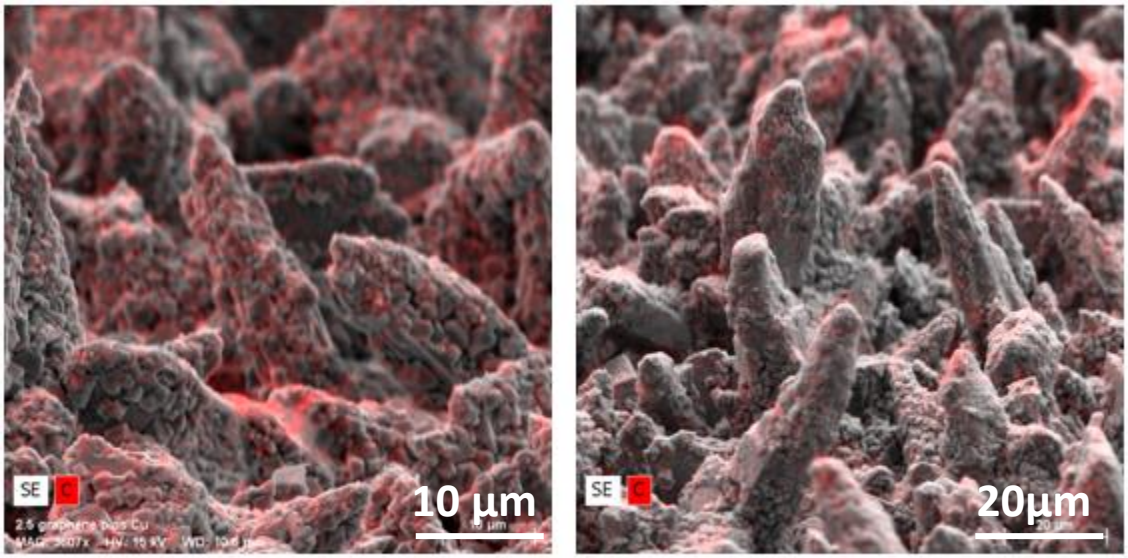

Figure 26: SEM image of GO- Cu electrodeposited chip 70° tilt Energy Dispersive X-ray Spectroscopy (EDS) showing carbon mapping (a) before the test (3.6 kX), (b) after the 20 tests (2.0 kX)

From Fig. 27, it is seen that the pore size of the structure has been changed marginally. Figure 27 show a top view of the sample. Figure 27 (a) is at the magnification of 5 kX while Fig. 27 (b) is at 2 kX magnification. Before starting the test, as seen in Fig. 27 (a), the structure was dense and average pore size was observed to be between 0.5 µm to 2 µm. 7But, after 20 runs, from Fig.27 (b), it is seen that size of the pores is increased from 2µm up to 6µm. Apart from this, the diameter of Bitter gourd structure is also decreased which suggests that the structure has become thinner.

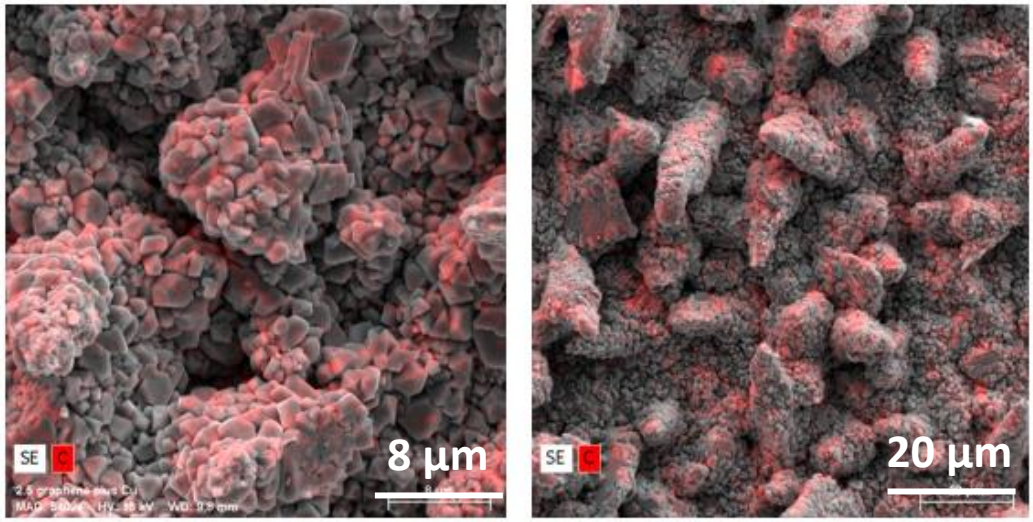

Figure 27: Top view of Energy Dispersive X-ray spectroscopy (EDS) showing carbon mapping (a) before (5.4 kX), (b) after 20 tests (2 kX)

4.2.4 Fourier Transform Infrared (FTIR)

Fourier Transform Infrared (FTIR) spectroscopy is an optical analytical technique used to identify the organic and inorganic compounds present on the surface. FTIR passes infrared radiation through samples and a detector plots the peaks of absorbance v/s wavenumber of the radiation. All matter contains the molecules and molecules have bonds. These bonds continually vibrate and move around when they are in a ground state. When these molecules are exposed to the radiation of exact same frequency as the energy difference between ground state and excited state, they get promoted to excited state. Hence, for a bond there is a designated wavenumber which absorbs that wavelength and thus the peak intensity in terms of absorbance is observed. [47]

For all the test surfaces, Fourier Transform Infrared (FTIR) spectroscopy (Shimadzu IR Prestige 21) was used to confirm the presence of copper and graphene oxide. Absorption peaks of bonds of molecules are observed at different energy levels indicating the presence of a particular compound. Absorption of IR by molecules is plotted against the wavelength. The different peaks signify the different bonds. Figure 28 shows the FTIR of 2.5% GO-Cu electrodeposited chip before the pool boiling test. The characteristic peaks of C=O including stretching vibration of carboxyl group at 1726 cm^{-1}, O-H deformation vibration resulting from C-OH at 1390 cm^{-1}, and C-O stretching vibration at 1032 cm^{-1} was observed here. The peak at 1570 cm^{-1} corresponding to the presence of aromatic rings (C=C) is also seen. The broad peak between 3400-3100 cm^{-1} is attributed to O-H stretching from water vapor. The C=C, C=O, C-OH peaks confirm the presence of GO on the surface. [48]

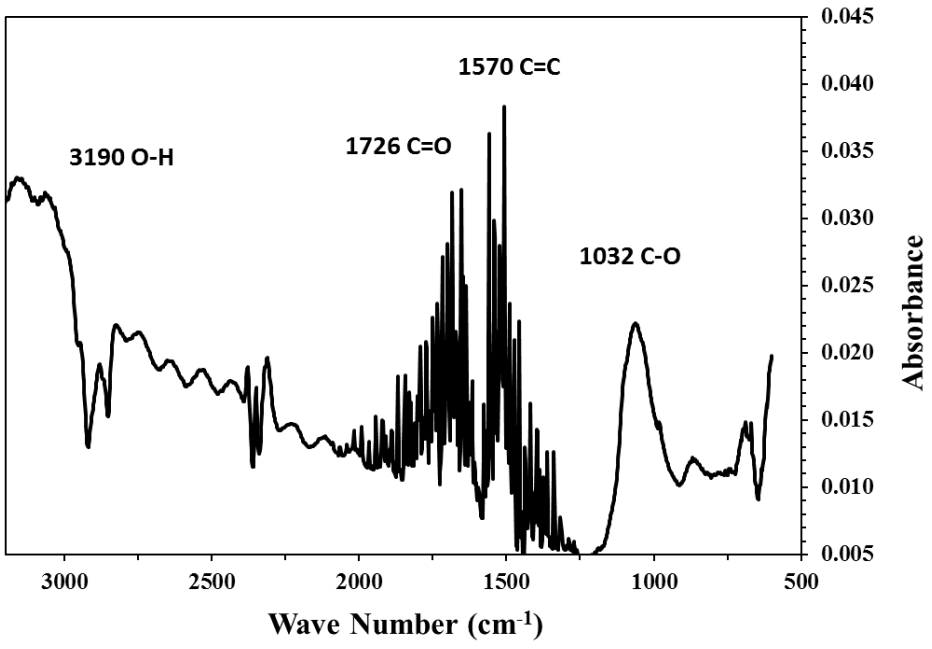

Figure 28: Fourier Transform Infrared (FTIR) of 2.5% GO-Cu electrodeposited chip (GS-4) before the pool boiling test

FTIR test was repeated on 2.5% GO-Cu electrodeposited chip after 20 runs. Data of the fresh test chip and aged test chip were plotted on the same graph to clearly visualize the difference between the peaks of new and aged chip. Figure 29 shows the combined plot of both fresh and aged chip. It is clearly seen that the aged chip traces the exact same path as that of the fresh chip, but with reduced intensity of the peaks. The peaks at wavenumbers 1570 and 1726 cm^{-1} indicated the presence of GO on the surface. [47] Hence, FTIR of aged chip confirms the presence of graphene on the test chip even after aging.

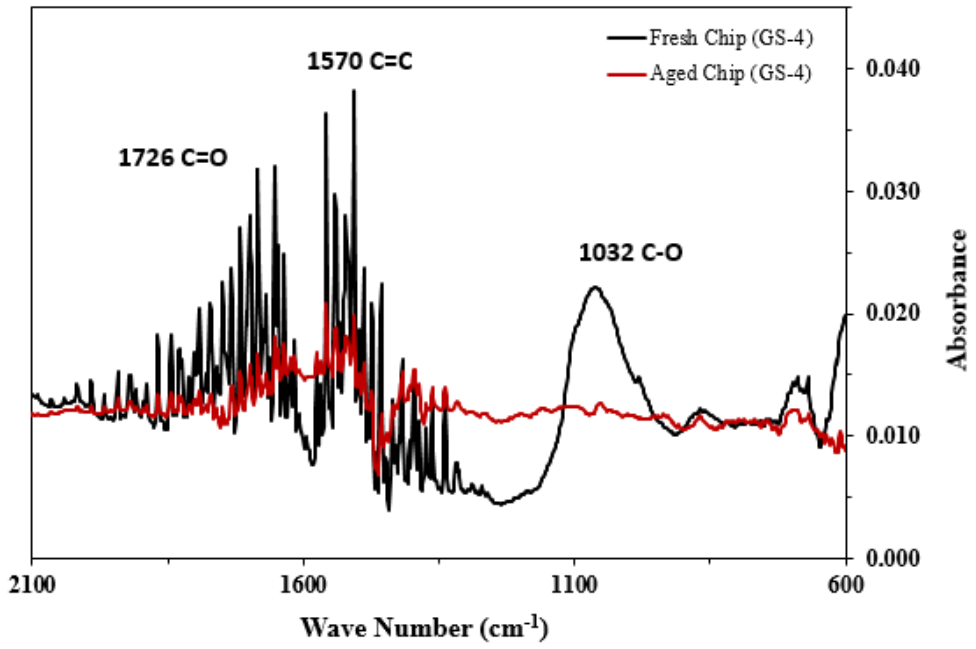

Figure 29:Fourier Transform Infrared (FTIR) of 2.5% GO-Cu electrodeposited chip (GS-4) chip before and after 20 pool boiling tests

4.2.5 X-Ray Diffraction (XRD)

X-ray diffraction is a technique used for determining the atomic and molecular structure of a crystal in which crystalline atoms cause a beam of X-rays to diffract in specific directions.

When X-rays are incident on the sample, incident beam get separated in transmitted beam and diffracted beam. The diffraction pattern is recorded in term of 2θ angle that indicates the crystalline phase of the material. The crystalline phases of the RIT G/GO coated substrates were investigated using a Rigaku DMAZ-IIB X-Ray Diffractometer (XRD) with Cu Kα radiation; wavelength 1.5418 Å. The spectra were recorded for 2θ ranges between 5° and 75° at a rate of 3°/min rate. The step size was 0.02° with an X-ray power of 40 kV and 35 mA. This range is expected to capture peaks from carbon and the underlying copper substrate. The location of characteristic peaks determines the presence of elements on the surface. XRD was taken for the 2.5% GO-Cu chip before any boiling test. Also, after 20 runs aging, XRD was done again.

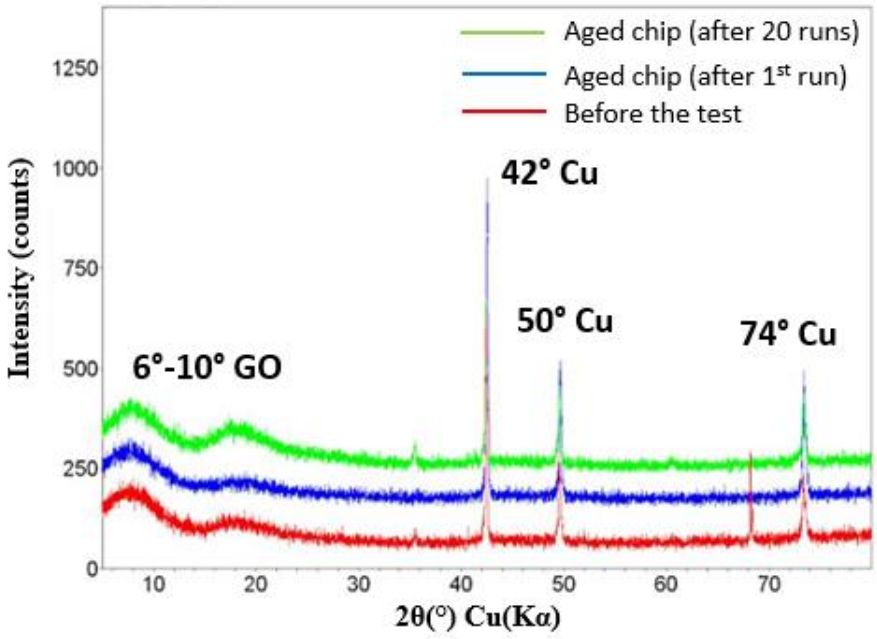

Figure 30: X-Ray Diffraction of fresh and aged chip of 2.5% GO-Cu electrodeposited chip (GS-4)

The peaks between 0 to 10°, show the presence of graphene oxide on the surface. All the peaks after 40° show the presence of copper. [48] It is interesting to observe that even after 20 repetitive cycles, the reduction of graphene from the surface was insignificant. indicating that the degradation of the pool boiling performance occurs due to increase in pore size (as explained in SEM), and is not because of the reduction of graphene oxide.

4.3 Results

4.3.1 Comparison of wall superheat and heat transfer performance

Due to continuous heating and cooling of plain copper chip (PC) and 2.5% GO-Cu electrodeposited chip (GS-4) during pool boiling, morphology of the surface changes that further affects the overall performance of the chips and the surface temperature. To compare the advantages of electrodeposition of metal and non-metal combination, aging test was performed on plain copper chip and the highest performing 2.5% GO-Cu (GS-4) electrodeposited chip.

Fig.31 shows the comparison of wall superheat temperatures at different stages of aging and it is clearly seen that for the same heat flux of ~80 W/cm², wall superheat of electrodeposited chip i.e. GS-4, is significantly less.

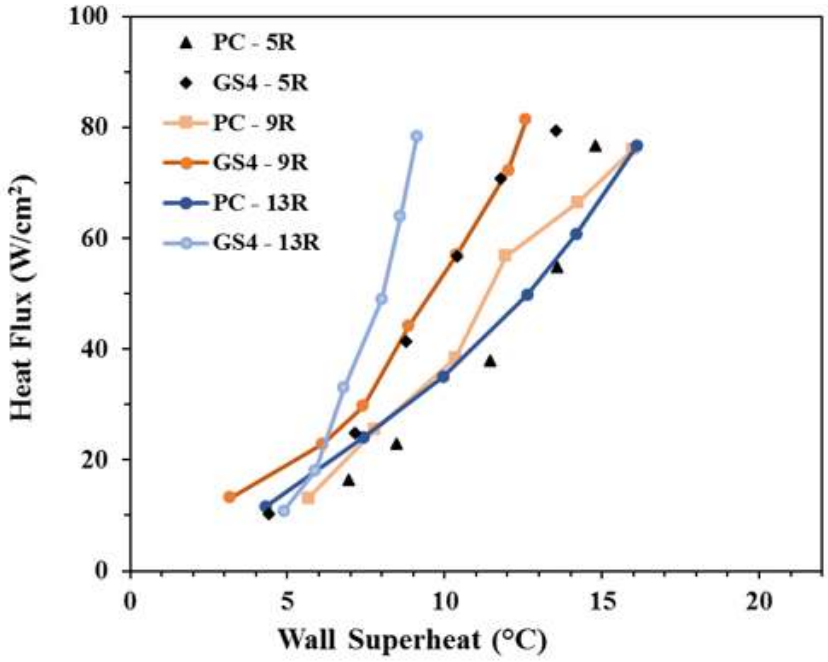

Figure 31: Comparison of wall superheat of Plain Copper chip (PC) and 2.5% GO-Cu electrodeposited chip (GS-4) at different repetitive test runs (R - repetition)

In the beginning of the pool boiling tests, both plain copper chip (PC) and 2.5% GO-Cu electrodeposited chip (GS-4) yielded similar performance with approximately same wall superheat of 80 W/cm² heat flux (1R to 3R). But, from the 5th repetitive test onward, wall superheat for GS-4 chip started to decrease (13.5°C), while wall superheat for plain copper chip increased (14.8°C) (as shown in Fig.31). At the 13th repetitive test, GS-4 chip produced as very low wall superheat of 9.1°C as compared to the plain copper chip that attained a wall superheat of 16.2°C.

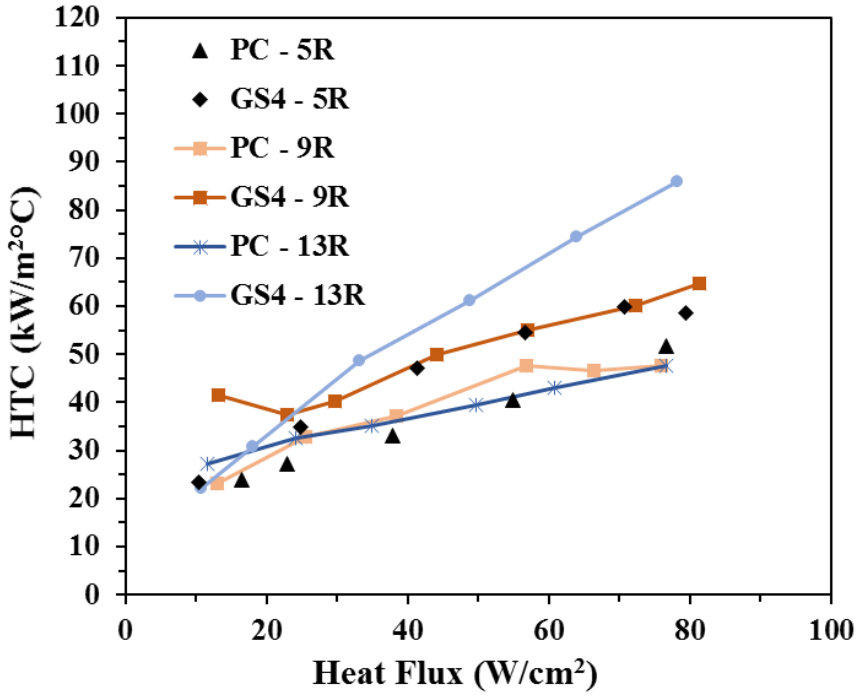

Figure 32: Heat transfer performance comparison of Plain Copper chip (PC) and 2.5% GO-Cu electrodeposited chip (GS-4) at different repetitive test runs (R - repetition)

Figure 32 shows the heat transfer performance for the compared runs. A maximum of 88 kW/m^2°C heat transfer coefficient was obtained for the GS-4 chip at 13th run at the heat flux of 80 W/cm^2. However, for the same number of repetitive test of plain copper chip, heat transfer coefficient was just 47 kW/m^2°C.

Figure 33 presents a comparison of the overall performance of aging of PC and GS-4 chips, and indicates the heat flux and wall superheats produced by the two chips during the second, tenth and the twentieth repetitive tests. It is observed that the heat transfer performance for GS-4 chip at any repetitive test is higher than that of the plain copper chip. After reaching the minimum of 9.1°C wall superheat on 13th repetitive test, the wall superheat slowly starts to increase. As seen from the Fig.33, at the end of twentieth repetitive test, wall superheat of GS-4 is 12°C, and that for the test chip PC, is 17.1°C. A

small rise in temperature of GS-4 after 13R is attributed to reduction in wicking rate and increase in range of cavity sizes. Figure 34 gives the heat transfer coefficient of the chips at initial, mid, and last repetitive test.

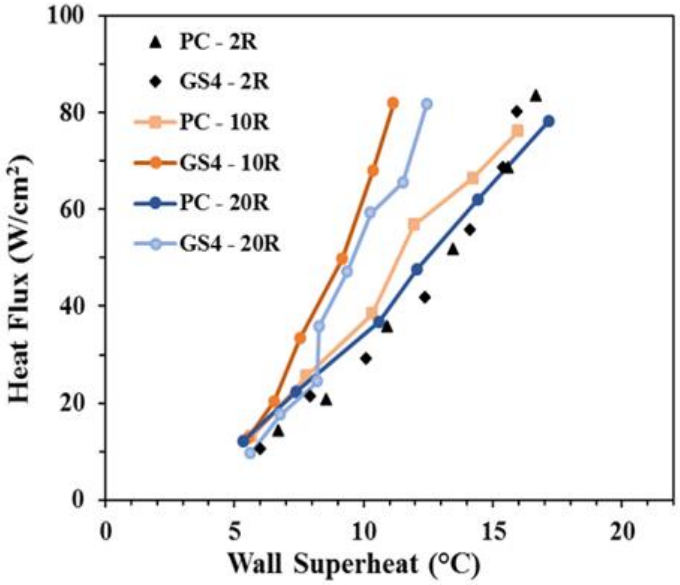

Figure 33: Comparison of wall superheat of Plain Copper chip (PC) and 2.5% GO-Cu electrodeposited chip (GS-4) at different (initial, mid and last repetitive test) repetitive test runs (R - repetition)

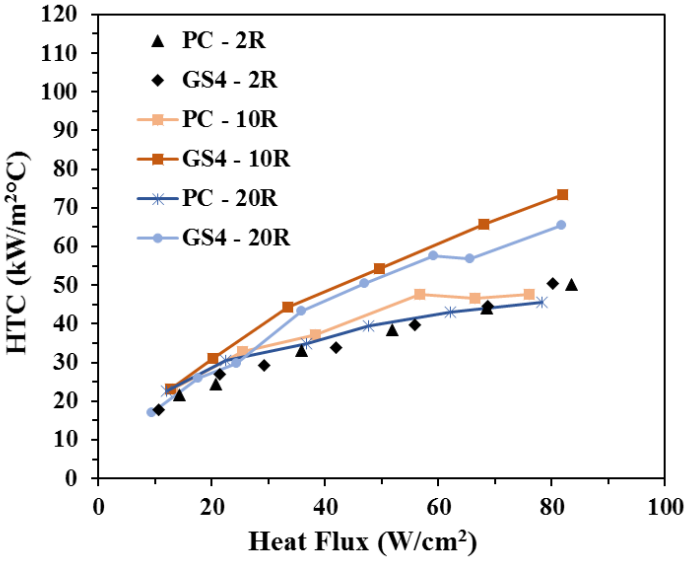

Figure 34: Comparison of heat transfer performance of Plain Copper chip (PC) and 2.5% GO-Cu electrodeposited chip (GS-4) at different (initial, mid and last repetitive test) repetitive test runs (R - repetition)

4.3.2 Comparison of CHF of fresh chip and aged chip

After performing 20 repetitive pool boiling tests, the aged chip was allowed to reach its CHF point. was taken till it reaches CHF. However, the plain copper chip was not tested to reach its CHF due to the heavy damage caused by the repetitive pool boiling tests. Figure 35 shows the pool boiling performance and comparison of the heat fluxes achieved by the plain and GS-4 chips. GS-4 chip was heated until its CHF and the recorded maximum heat flux was found to be 146 W/cm² with respective wall superheat of 13.3°C. The pristine GS-4 chip had maximum heat flux of 220 W/cm² at wall superheat of 15.2°C. Despite, the aging, the electrodeposited 2.5% GO-Cu chip yielded higher CHF with better pool boiling performance compared to the aged and fresh plain copper chip

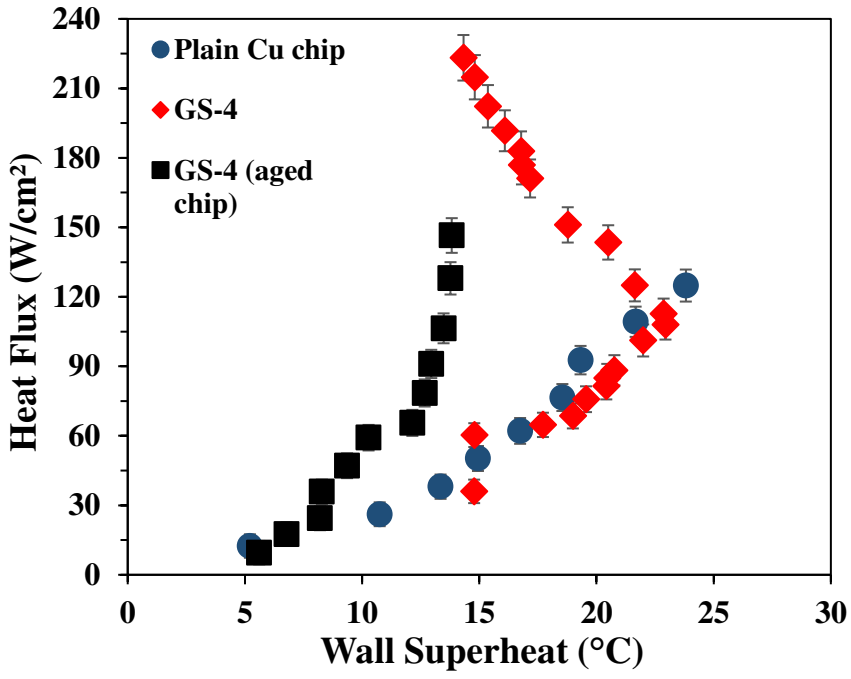

Figure 35: Comparison of CHF of aged and non-aged 2.5% GO-Cu electrodeposited chip (GS-4)

Figure 36 shows the heat transfer performance of fresh chip and aged chip. It is observed that the performance of the GS-4 chip decreases with increase in number of repetitive tests. However, HTC of aged GS-4 chip is much higher than that of the plain copper chip. Compared to plain chip, fresh GS-4 chip improved the heat transfer performance by ~195% while the aged chip improved the performance by ~102%. Table 6 summarizes the CHF and HTC of the aged and non-aged chips.

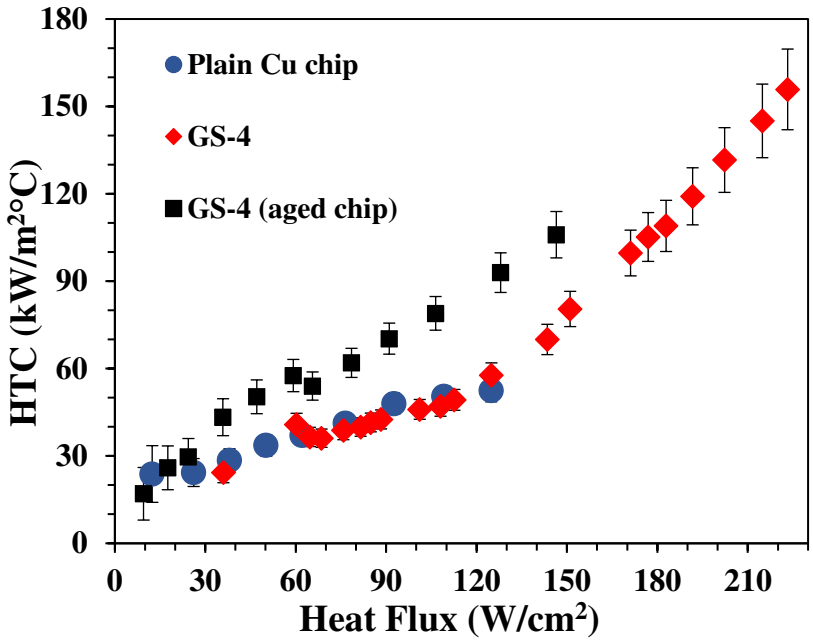

Figure 36: Comparison of heat transfer performance of fresh and aged Plain Copper chip (PC) and 2.5% GO-Cu electrodeposited chip (GS-4)

Table 6: CHF and HTC comparison of fresh and aged chip of 2.5% GO-Cu (GS-4)

Chip	CHF (W/cm²)	Wall superheat (°C)	HTC (kW/m²°C)
Plain Cu chip	125	23.8	52.5
2.5% GO-Cu (GS-4)	220	14.3	155
2.5% GO-Cu(GS-4) (aged chip)	141	13.3	106.2

4.3.3 Effect of aging the morphology

Due to continuous heating and cooling of the chip during and after pool boiling test, the morphology of the test surface underwent various changes. First important observation was that, the contact angle and wickability of the surface changed. The volumetric change in a liquid droplet of a fixed volume was captured for a duration of ~80 s using a VCA Optima goniometer. The coating exhibited poor wickability as seen by the low volume of liquid wicked into the coatings. From Fig.24 the characterization section, it is clearly observed that wicked fluid is very less since the contact angle remains higher after a same time as compared to the contact angle before the test. Hence, due to reduction in wicking rate, CHF of the aged chip decreases. Also, from table 5, it can be seen that coating has lost its hydrophilicity and the has become a hydrophobic surface.

4.3.4 Enhancement mechanism of aged GS-4 chip

Although the heat flux after 20 tests has reduced, it is still higher than the plain copper chip. The enhancement mechanism of this structure is primarily due to the increased nucleation site density. The range of cavity sizes (1-20µm) available for nucleation both in the planar and along the coating thickness is identified as the main contributing mechanism for the increase in HTC that causes the boiling curve to shift to the left owing to the rapid nucleation activity. On the other hand, the wicking rate of the structure was found to be decreasing from 1.7 to 0.9 mm/s, indicating that the liquid retention in the wicking structures did not contribute to the enhancement. It is postulated here that the GO encapsulates the porous copper thereby inhibiting liquid to be wicked into the coatings which was evident from the low CHF values observed for these samples. [8] [43]

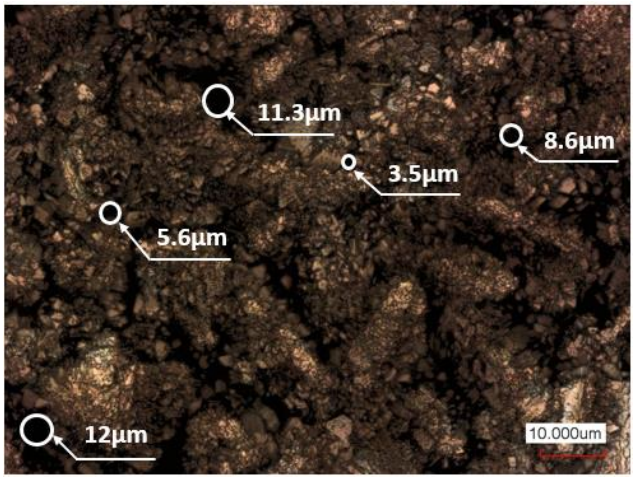

Figure 37: Confocal laser scanning image showing range of cavities available for nucleation in the samples

Chapter 5

Chapter 3 and 4 describe the enhancements and longevity of the performance achieved from 2 step electrodeposition process and advantages of use of Graphene in terms of heat transfer performance and aging as well. From the literature review in chapter 2 it is indicated that the porous surfaces provide additional nucleation sites that aid in reducing the wall superheat. Chapter 5 centers on enhancing the heat transfer performance by a newly developed electrodeposition technique involving a variable multi-step electrodeposition of copper on the plain copper chip. The objective of the proposed new multi-step electrodeposition technique is to improve the bonding of the deposited material with the base material and simultaneously improve the heat transfer performance of the test surface and reduce the wall superheat.

The scope of this chapter is to – a) obtain the CHF data of the new multi-step electrodeposited chip and compare the recorded values with the CHF of the previously studied two step deposited copper chip, and b) conduct the aging study on both two step and multi-step electrodeposition of copper on copper chips. This new multi-step electrodeposition process has never been implemented before which further strengthens the claim of the work presented in this chapter.

5.1 Development of new electrodeposition technique

Based on the pool boiling analysis it was observed that the coatings obtained by two-step deposition method were not sustainable and would peel off with after just one pool-boiling

tests. To address, this issue a six-step procedure was devised to improve the longevity and performance of the electrodeposited chip.

The six-step method was similar to the previously employed two-step electrodeposition technique, and followed the Galvanostatic method for deposition. The key difference between the two methods is the alternate deposition and strengthening of the bonds of the deposited layer in the case of six-step method. The formation of deposited layer in smaller increments allows the strengthening of the deposition. In contrast, the two-step technique only involved the deposition by the supply of a higher current density for a short duration, followed by the lower current density for a longer duration. In the first step, deposition of copper along with simultaneous evolution of hydrogen bubbles occurs, leaving behind porous copper. In the second step, the current density is taken such that the copper is deposited without evolution of hydrogen bubbles. This improves the bonding and the porosity of the copper surface.

In order to build more robust deposition, this same technique of higher current density for short duration which involves evolution of hydrogen bubbles and small current density for longer duration is used. But, instead of supplying a large current continuously for 15 sec., it is divided in 3 steps followed by a small current for longer period after each small step of large current density. The overall time of higher current density is kept constant but is divided in the intervals of 5 sec. Table 7 below summarizes the steps involved in six-step deposition process along with the applied current density and its duration for each step.

Table 7: Six-step electrodeposition process

Step #	Current density (mA/cm^2)	Time (sec.)
Step 1	400	5
Step 2	40	2500
Step 3	400	5
Step 4	40	2500
Step 5	400	5
Step 6	40	2500

The electrolyte solution used for this deposition was 0.8M $CuSO_4$ (5.85 gm) and 1.5M conc. H_2SO_4 (3.14 mL) and 40mL distilled water. For this six-step deposition, same electrolyte solution and electrodeposition procedure was followed as mentioned in Chapter 3. Due to heavy damage on two-step deposited chip, both the chips were tested 7 repetitive times before taking to CHF.

5.2 Characterization

5.2.1 Contact angle study

Similar to the studies published in Chapter 3 and 4, the static, advancing and receding contact angles for the newly synthesized chips were also recorded. Table 8 summarizes the contact angles measured for fresh and aged chips.

Table 8: Contact angles of Two Step (TS) and SS (Six-Step) electrodeposited copper on copper chips (fresh and aged chips)

Test Chip	Before the test				After 7 runs			
Cu on Cu (Two Step deposition) (TS)	Static	Advancing	Receding	Hysteresis	Static	Advancing	Receding	Hysteresis
	53	67	18.4	48.6	80	98	21.3	76.7
Cu on Cu (Six Step deposition) (SS)	16	29.6	9.9	19.7	128.5	137	49.4	106.4

5.2.2 Wicking rate

The wicking rates for both Two-Step and Six-Step chips were measured using a VCA Optima Goniometer. As shown in Fig. 38, for the time frame of ~80 seconds, contact angle reduction for Six-Step (SS) deposited chip is much higher as compared to Two-step (TS) deposited chip. Contact angle for SS chip reduced from 45° to almost 16° within 80 seconds showing that wicking rate for SS is way higher than TS. The wicking rates of each surface was measured by visualizing the dynamic spreading behavior of a drop placed on these surfaces.

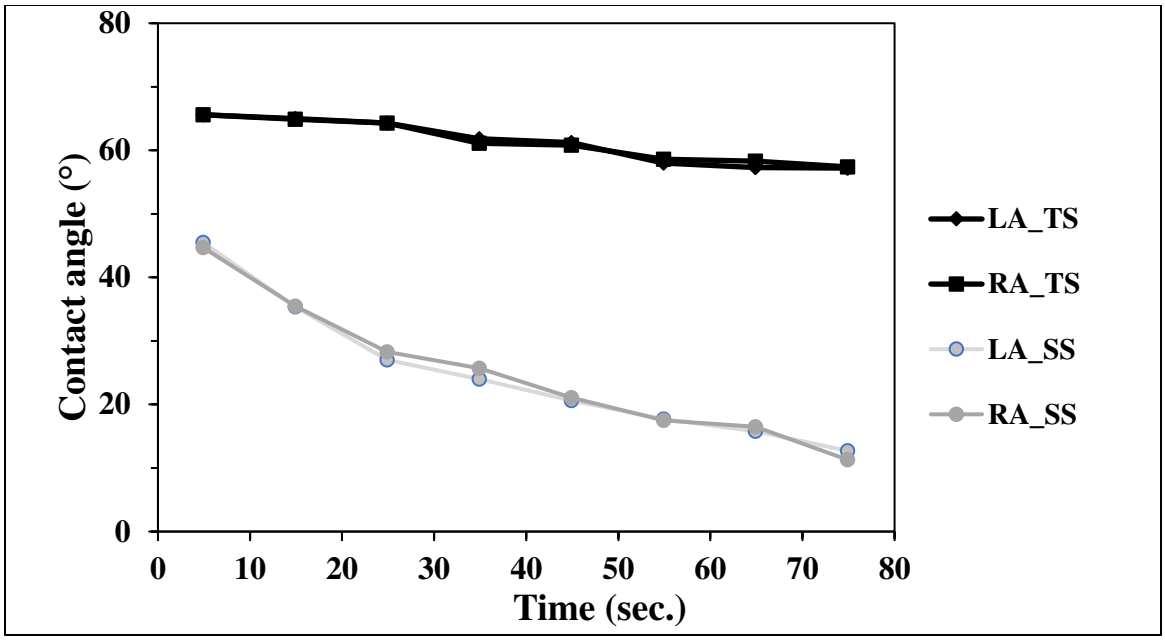

Figure 38: Change in contact angle over time of left and right side of the droplet (LA and RA respectively) for Two-Step (TS) and Six-Step (SS) electrodeposited chips

5.2.3 Scanning Electron Microscope (SEM)

The morphology of the substrates was studied by JSM-6400V scanning electron microscope (SEM), JEOL, Ltd., Tokyo, Japan at an accelerating voltage of 15 kV. Accelerating voltage represents the energy that is set to accelerate the electrons in the electron beam when shooting on the sample. The WD on the SEM image represents the working distance between sample and the lens and it is zoomed to a required magnification from this WD. SEM MAG tells that whatever the image is shown, is magnified 5000 times. As higher magnification, view field reduces. It can be observed in Fig.39, that for the magnification of 5kX, view field is just 41.4µm.

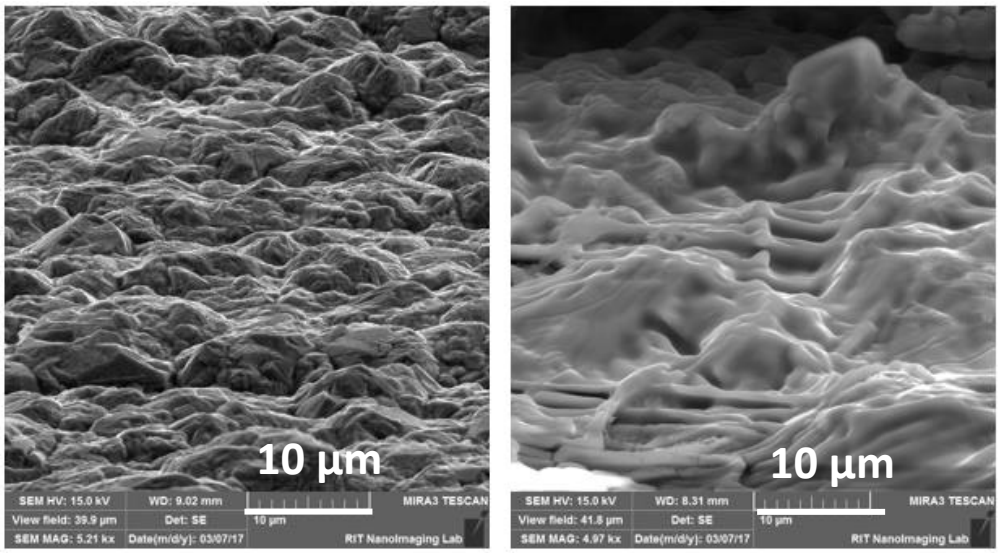

(a) (b)

Figure 39: Scanning Electron Microscope (SEM) images of the electrodeposited chips using Galvanostatic method, 5kX, 70° tilt (a) Cu on Cu two-step deposition, (b) Cu on Cu six-step deposition, 10µm

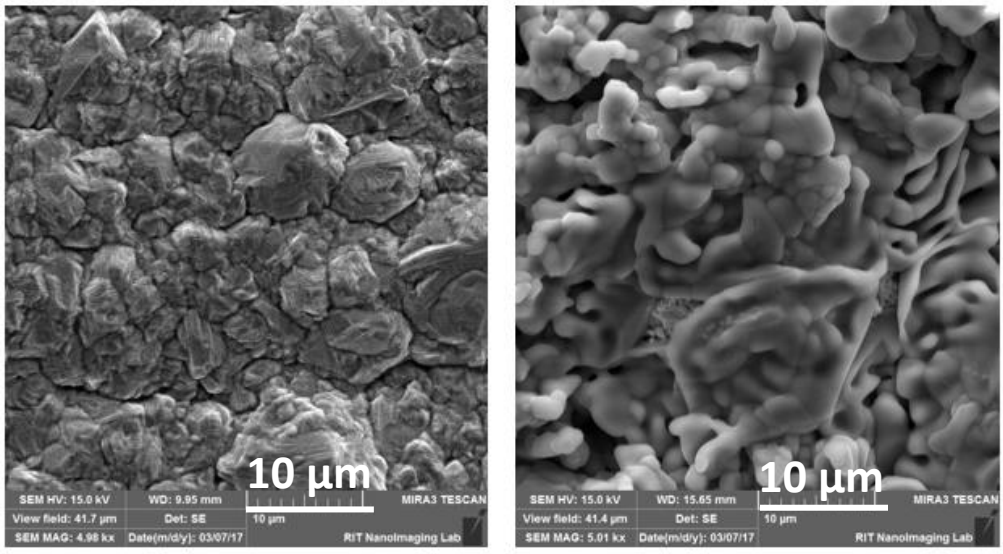

(a) (b)

Figure 40: Top view of copper on copper electrodeposited chip, 5kX, scale 10 µm, (a) two-step, (b) six-step

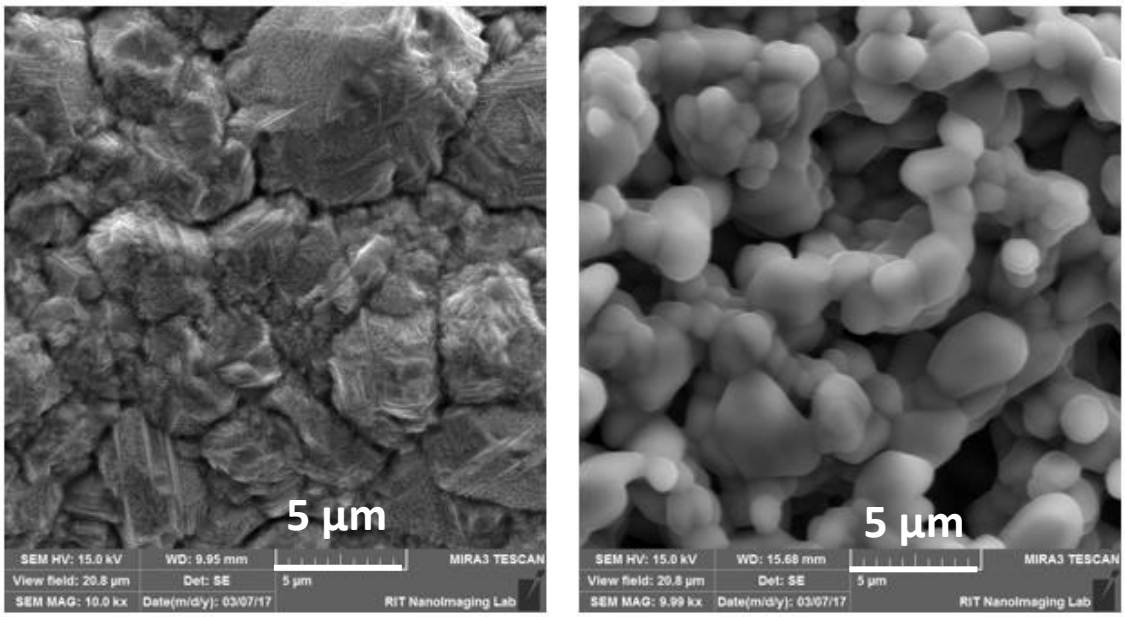

(a) (b)

Figure 41: SEM image of top view of copper on copper electrodeposited chip showing the structure at 5µm with 10kX magnification (a) two-step deposition, (b) six-step deposition

Figure 39 of SEM as shown above is obtained by tilting the stage at 70° Figures 40 and 41 are the top views of the test chip. From Fig.39, it is observed that the thickness of the deposition is higher for six step deposited surface as compared to two step deposited surface. For Fig. 39(a) of two step deposited copper, the thickness of the coating is approximately 2-3µm while that of the six-step deposited surface (Fig. 39(b)) is around 8-10 µm.

Compared to six step deposited coating (2-3 µm), the two-step deposited coating did not show any pores. Figure 41 shows the top view of the morphology of TS and SS deposited chips at the magnification of 10kX. Highly microporous structure is formed from six step deposited chip. Pores in the range of 0.5 µm to 3 µm are formed. Compared to Fig.41 (b), Fig. 41(a) has no porosity.

5.3 Results

Results section consists the enhancement due to newly employed six step electrodeposition technique and its comparison with plain chip and existing results. In addition to this, the aging study of the six-step deposited chip is carried along with two step deposited chip to compare the results.

5.3.1 CHF and HTC Enhancement due to new electrodeposition technique

Figure 41 shows the pool boiling curves obtained with the two-step deposited chip (TS) and six-step deposited chip (SS). The deposition was carried out in a carefully designed electrochemical cell using a Galvanostatic method as discussed previously. TS chip reached a CHF of 150 W/cm² at a wall superheat of 18.7°C. A CHF of 192 W/cm² was obtained with SS at a wall superheat of 18.8°C. For the electrodeposition of copper on copper, this is the highest heat flux value that has been ever reported. The test surface of six step deposited chip resulted in an increase in CHF with a simultaneous reduction in wall superheat. Plot 41 shows the comparison of CHF of six step deposited chip with the CHF from literature.

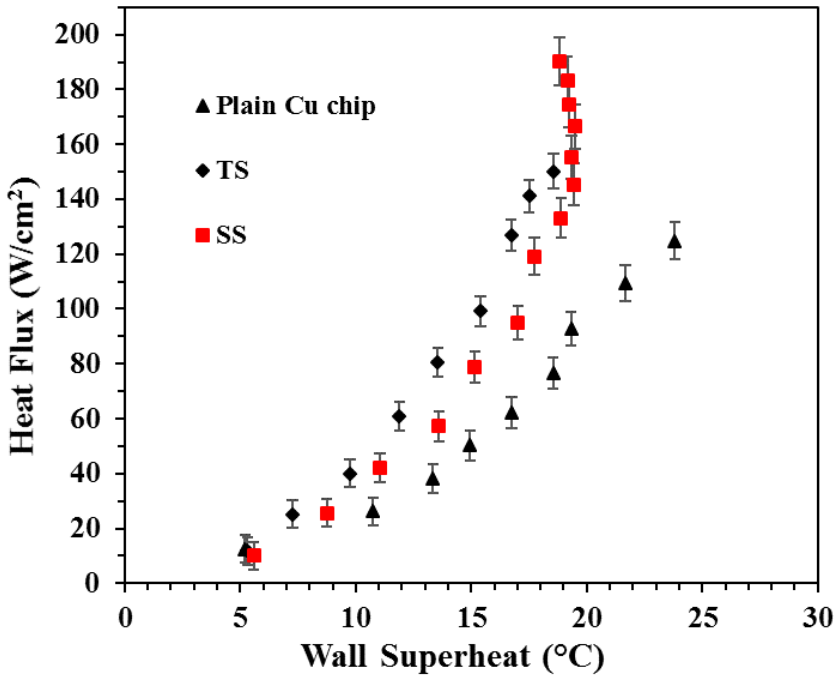

Figure 42: Comparison of CHF of Two-Step (TS) and Six-Step (SS) electrodeposited chips

Figure 42 shows the comparison of HTC of TS and SS obtained for the surfaces prepared using the Galvanostatic process. A maximum HTC of 102 kW/m^2°C was achieved for Six-Step deposited chip, while for two step deposited chip, HTC of 78 kW/m²°C was achieved. By implementing the new six step electrodeposition technique, 53% enhancement in CHF was achieved while ~96% enhancement in heat transfer coefficient was observed.

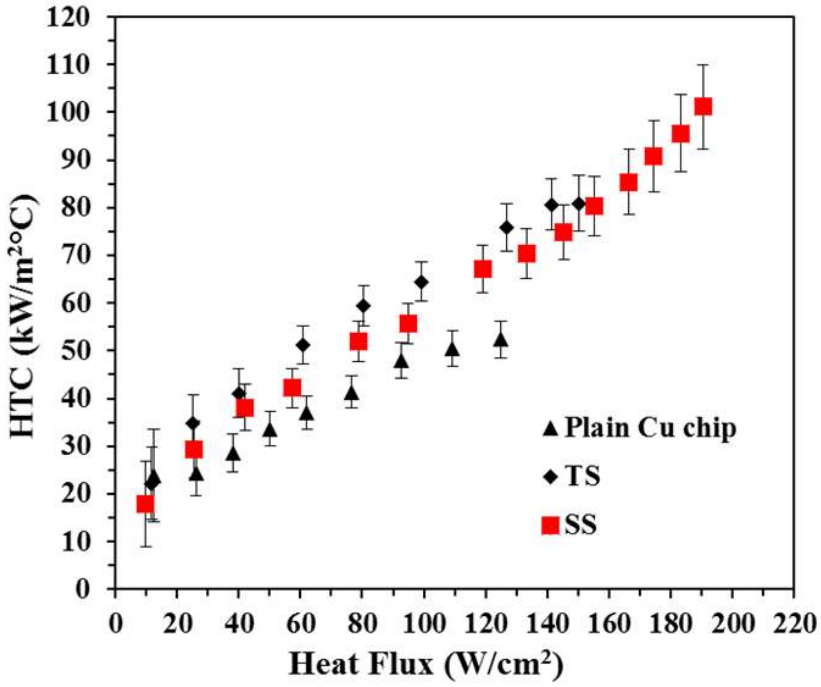

Figure 43: Comparison of heat transfer performance of Two-Step (TS) and Six-Step (SS) electrodeposited chips

5.3.2 Comparison of wicking rate

The wicking rates play a significant role in enhancing the CHF. In the samples investigated here (Two-Step and Six-Step deposited chips), the HTC is significantly increased for six-step deposited chip due to the low wall superheats at relatively higher heat fluxes. SS in addition to wicking, have increased nucleation sites that are activated under suitable superheat conditions and contribute towards decreasing the wall superheat. The mechanism for such a trend is attributed to the range of cavity sizes available for nucleation as discussed previously in Chapter 3. The nucleation activity is further promoted by the enhanced evaporation through microlayer partitioning mechanisms. This arrangement results in an increase in both CHF and HTC characteristics demonstrated here. The effect

of additional nucleation sites and wicking are the main contributing mechanisms in enhancement.

5.3.3 Test surfaces of the aged chips

Due to continuous pool boiling testing, morphology of the test surface gets affected which results in reduction in performance of the chip. At the end of 3rd repetitive test, it was observed that the test surface of two step deposited chip had started to damage and the coating had come off partially. But, after performing 7 repetitive pool boiling tests, the coating of the two-step (TS) deposited chip was destroyed completely. However, the coating of six-step (SS) deposited chip was not reduced at all. Hence, it can be said that the new multi-step electrodeposited chip has better bonding and the adhesion of the deposition to the surface is very strong.

Figure 44 shows the photographic images of the surfaces of the aged chips. It is clearly seen from Fig.44 (a) that the coating of the surface of two step deposited chip has completely come off. Compared to that, coating of the six-step deposited chip is still present, indicating that bonding is better for six step deposited chip.

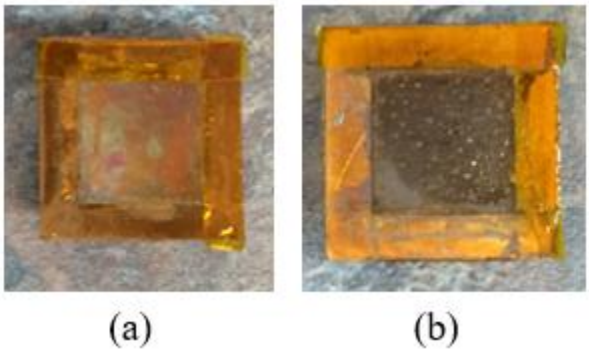

Figure 44: Test surface of aged (a) Two-Step (TS), (b) Six-Step (SS) electrodeposited chips

5.3.4 Effect of aging on wall superheat and heat transfer performance

To compare the advantages of the newly employed electrodeposition techniques in terms of longevity and adhesion improvement, aging study was carried out. Fig.45 shows the comparison of wall superheat temperatures at different stages of aging that indicates that for the same heat flux of ~80 W/cm^2, wall superheat of six-step electrodeposited chip i.e. SS, is significantly less than that of the two-step (TS) deposited chip.

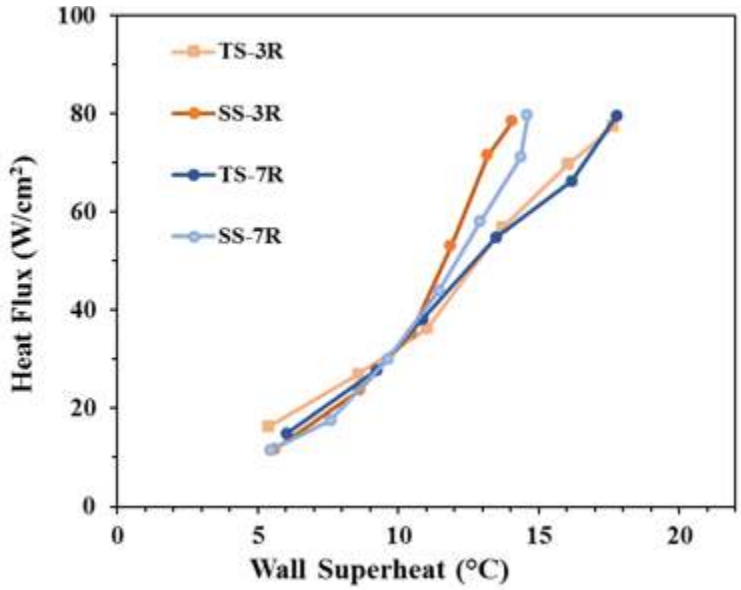

Figure 45: Comparison of wall superheat of Two-Step (TS) and Six-Step (SS) copper on copper electrodeposited chips at different repetitive test runs (R – repetition)

For the 3rd repetitive test, as shown in plot, for the same heat flux, wall superheat of TS chip is 17.6°C while that of the SS chip is 14.3°C. Again, the similar trend is observed in all the tests. (4R to 7R).

Figure 46 shows the heat transfer coefficient comparison of TS and SS chips. Maximum of 60 kW/m²°C HTC was obtained for SS chip at the 3rd repetitive test, while 44 kW/m²°C

HTC was obtained for the TS chip at 3rd repetitive test. It is observed that, for a given heat flux, the HTC of SS chip is always higher than TS chip. This indicates that Six-Step (SS) deposited chip has higher heat transfer efficiency than that of the Two-Step (TS) deposited chip.

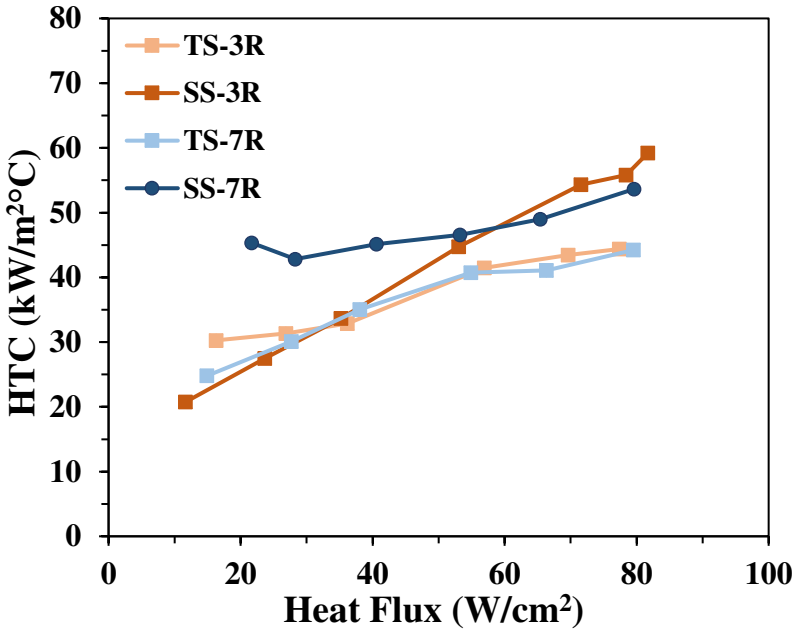

Figure 46: Comparison of heat transfer performance of Two-Step (TS) and Six-Step (SS) copper on copper electrodeposited chips at different repetitive test runs (R – repetition)

5.3.5 Effect of aging on CHF and HTC

As explained earlier, due to heavy damage of the TS chip, the CHF obtained for TS is exaggerated. Fig.47 shows the CHF of the aged chips. Compared to first CHF value, aged chips have less CHF. Wall superheat of TS chip is increased as well. However, for the SS chip, wall superheat temperature has remained similar as that of mentioned in 5.3.1 section.

CHF of 152 W/cm² was obtained for the aged SS chip at wall superheat of 18.8°C, while CHF of 140 W/cm² at a wall superheat of 23°C was obtained for TS chip.

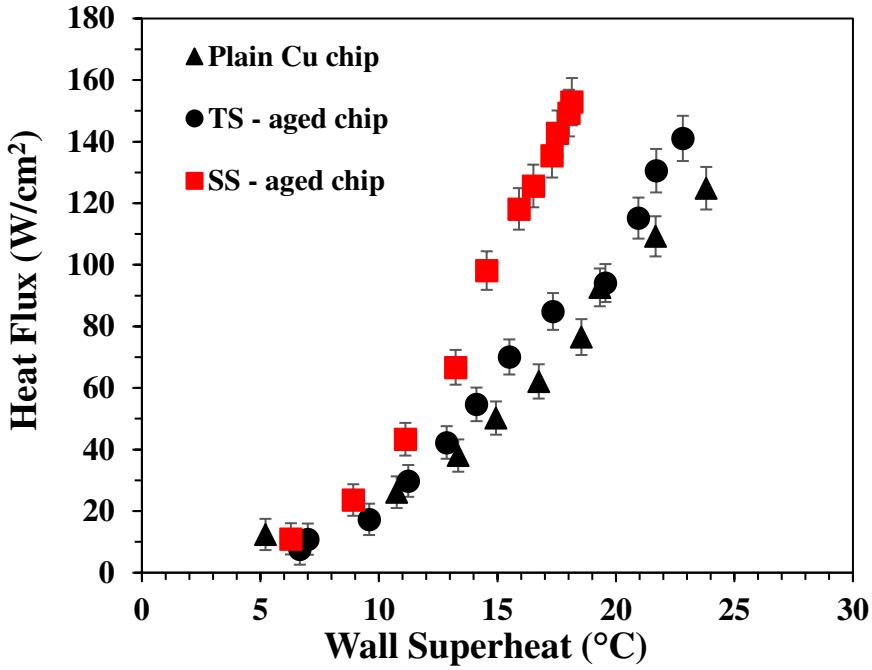

Figure 47: Comparison of CHF of Two-Step (TS) and Six-Step (SS) copper on copper electrodeposited chips

HTC of 84 W/m² °C was achieved for SS chip at the CHF, while for the TS chip, it was 61 W/m² °C. Compared to HTC of fresh samples, HTC and CHF of the aged chips reduced. However, newly employed Six-Step electrodeposited chip performed better than two step deposited chip. CHF, wall superheat and hence HTC of the SS chip is higher than TS indicating the improvement in performance due to new electrodeposition technique.

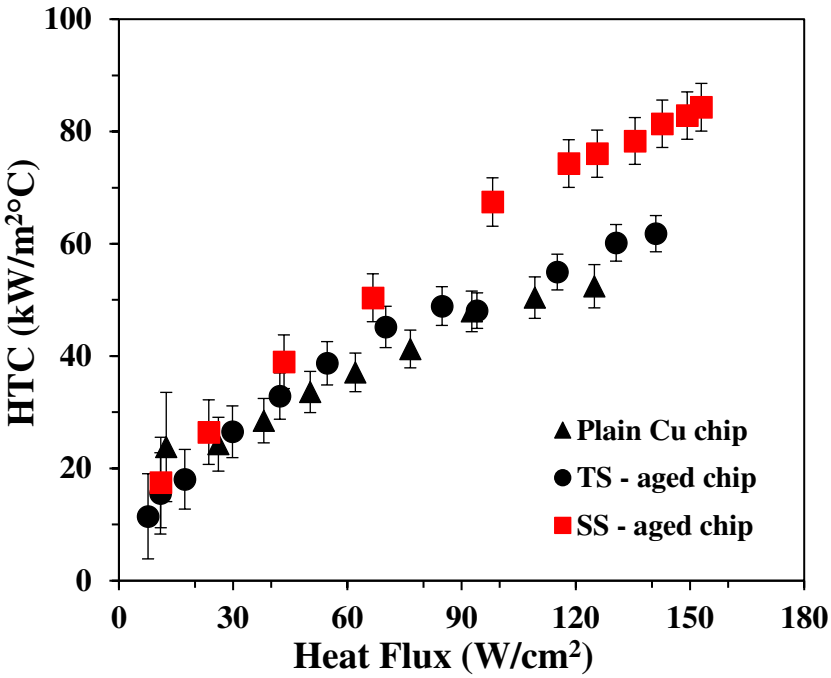

Figure 48: Comparison of HTC of Two-Step (TS) and Six-Step (SS) copper on copper electrodeposited chips

Chapter 6

6.1 Conclusions

This research work was divided into two parts. For the first part, aim was to enhance the heat flux by reducing wall superheat. The following conclusions were drawn from the part one:

1) Two step electrodeposition technique was employed with the combination of a metal (Copper) and a non-metal (Graphene Oxide).
2) For 2.5% by volume of Graphene Oxide in 40mL electrolyte solution, (GS-4), CHF of 220W/cm² was achieved at wall superheat of 14.2°C. Compared to plain copper chip, ~76% enhancement in heat flux was achieved using 2.5% GO.
3) It was observed that as the percentage of GO in an electrolyte goes on increasing, heat flux also goes on increasing.
4) When GS-4 chip was tested for the longevity and aging, after overall 85 hours of pool boiling testing, pool boiling performance of the chip was still higher than that of the plain copper chip. CHF of 146 W/cm² was achieved at wall superheat of 13.3°C. Plain copper chip could not sustain the continuous pool boiling tests and the surface of the plain copper chip was heavily damaged.
5) Surface characterization techniques including Scanning Electron Microscope (SEM), Fourier Transform Infrared (FTIR), and X-Ray Diffraction (XRD) confirmed the presence of Graphene Oxide on the surface even after aging. This shows that bonds between the graphene oxide and copper are strong and were helpful in improving the pool boiling performance.

In the second part, a new multi-step electrodeposition technique was employed to improve the aging by improving adhesive bond strength and to improve the pool boiling performance as well. Following conclusions were drawn from the study:

1) In the new Multi-step electrodeposition technique of copper on copper, alternate activity of deposition and strengthening the deposition was performed which enhanced the adhesive and cohesive bonding of the deposition.
2) Scanning Electron Microscope (SEM) confirmed the drastic change and improvement in the morphology of the six-step electrodeposited surface.
3) CHF of 192 W/cm² at wall superheat of 18.8°C was achieved for the six-step deposited chip, which is 149 W/cm² for two-step deposited chip. Hence, ~30% enhancement was achieved by using new six-step electrodeposition technique as compared to two-step deposited chip.
4) When both two-step (TS) and six-step (SS) deposited chips were taken for the aging test, the SS chip performed better than TS chip. The coating of TS chip came off after 6 repetitive pool boiling tests, while the coating of SS chip did not come off even after hitting the CHF.
5) Improvement in wicking and increased nucleation sites were the critical factors in improving the critical heat flux of the six-step deposited chip.

6.2 Future work

A systematic parametric study of different current densities and different deposition time periods can be performed to optimize the pool boiling performance. The new six-step electrodeposition technique can be employed by adding Graphene Oxide in an electrolyte solution. As seen in Chapter 5, six-step electrodeposition gives very high CHF performance at low wall superheats. Hence, the use of graphene oxide will ensure the reduction in wall superheat and improved pool boiling performance.

Implementation of six-step deposition process on microchannel surfaces can make a huge impact in the field of electronics cooling. Microchannel test surfaces with multi-step selective electrodeposition will improve the CHF to a very high extent and will simultaneously reduce wall superheat.

Due to enhanced bonding, test surface will definitely last very long and will give high performance. Apart from this, porosity of six-step electrodeposited surfaces can further be controlled and varied by varying the deposition time and current density.

6.3 References

[1] Honda, H., and Wei, J. J., 2004, “Enhanced Boiling Heat Transfer from Electronic Components by Use of Surface Microstructures,” Exp. Therm. Fluid Sci., 28(2–3), pp. 159–169.

[2] Xu, J., Ji, X., Zhang, W., and Liu, G., 2008, “Pool Boiling Heat Transfer of Ultra-Light Copper Foam with Open Cells,” Int. J. Multiph. Flow, 34(11), pp. 1008–1022.

[3] “Wolverine Tube INC.,2006, Boiling heat transfer on external surfaces, engineering data book

[4] Kumar, G., 2014, “An Analysis of Various Thermo-Fluid Properties during Boiling Heat Transfer in Microchannels.”

[5] Kandlikar, Satish G., and Paul H. Spiesman. 1998, "Effect of surface finish on flow boiling heat transfer." ASME Heat Transfer Div Publ HTD 361: 157-163.

[6] “Lecture 12 Electrodeposition.pdf.”

[7] Schwarzacher, W., 2006, “Electrodeposition: A Technology for the Future,” Electrochem. Soc. Interface, 15(1), pp. 32–33.

[8] Jaikumar, A., Kandlikar, S. G., and Gupta, A., 2017, “Pool Boiling Enhancement through Graphene and Graphene Oxide Coatings,” Heat Transf. Eng., 38(14–15), pp. 1274–1284.

[9] Jaikumar, A., Santhanam, K. S. V., Kandlikar, S. G., Raya, I. B. P., and Raghupathi, P., 2015, “Electrochemical Deposition of Copper on Graphene with High Heat Transfer Coefficient,” ECS Trans., 66(30), pp. 55–64.

[10] Shin, H.-C., and Liu, M., 2004, “Copper Foam Structures with Highly Porous Nanostructured Walls,” Chem. Mater., 16(25), pp. 5460–5464.

[11] Patil, C. M., and Kandlikar, S. G., 2014, “Review of the Manufacturing Techniques for Porous Surfaces Used in Enhanced Pool Boiling,” Heat Transf. Eng., 35(10), pp. 887–902.

[12] Albertson, C. E., 1977, *Boiling Heat Transfer Surface and Method*, Google Patents.

[13] Pop, E., Varshney, V., and Roy, A. K., 2012, "Thermal Properties of Graphene: Fundamentals and Applications," MRS Bull., 37(12), pp. 1273–1281.

[14] Fuhrer, M. S., Lau, C. N., and MacDonald, A. H., 2010, "Graphene: Materially Better Carbon," MRS Bull., 35(4), pp. 289–295.

[15] Chyu, M. C., 1982, "Characteristics of Nucleate Pool Boiling from Porous Metallic Coatings," J. Heat Transf., 104, p. 279.

[16] Wojcik, T. M., 2009, "Experimental Investigations of Boiling Heat Transfer Hysteresis on Sintered, Metal Fibrous, Porous Structures," Exp. Therm. Fluid Sci., 33(3), pp. 397–404.

[17] Mori, S., and Okuyama, K., 2009, "Enhancement of the Critical Heat Flux in Saturated Pool Boiling Using Honeycomb Porous Media," Int. J. Multiph. Flow, 35(10), pp. 946–951.

[18] Patil, C. M., and Kandlikar, S. G., 2014, "Pool Boiling Enhancement through Microporous Coatings Selectively Electrodeposited on Fin Tops of Open Microchannels," Int. J. Heat Mass Transf., 79, pp. 816–828.

[19] WEBB, R. L., 1983, "Nucleate Boiling on Porous Coated Surfaces," Heat Transf. Eng., 4(3–4), pp. 71–82.

[20] Weibel, J. A., Garimella, S. V., and North, M. T., 2010, "Characterization of Evaporation and Boiling from Sintered Powder Wicks Fed by Capillary Action," Int. J. Heat Mass Transf., 53(19–20), pp. 4204–4215.

[21] Iverson, B. D., Davis, T. W., Garimella, S. V., North, M. T., and Kang, S. S., 2007, "Heat and Mass Transport in Heat Pipe Wick Structures," J. Thermophys. Heat Transf., 21(2), pp. 392–404.

[22] Li, Q., Wang, W., Oshman, C., Latour, B., Li, C., Bright, V. M., Lee, Y.-C., and Yang, R., 2011, "Enhanced Pool Boiling Performance on Micro-, Nano-, and Hybrid-Structured Surfaces," ASME, pp. 633–640.

[23] Kandlikar, S. G., 2001, "A Theoretical Model to Predict Pool Boiling CHF Incorporating Effects of Contact Angle and Orientation," J. Heat Transf., 123(6), p. 1071.

[24] Betz, A. R., Xu, J., Qiu, H., and Attinger, D., 2010, "Do Surfaces with Mixed Hydrophilic and Hydrophobic Areas Enhance Pool Boiling?," Appl. Phys. Lett., 97(14), p. 141909.

[25] Betz, A. R., Jenkins, J., Attinger, D., and others, 2013, "Boiling Heat Transfer on Superhydrophilic, Superhydrophobic, and Superbiphilic Surfaces," Int. J. Heat Mass Transf., 57(2), pp. 733–741.

[26] O'Hanley, H., Coyle, C., Buongiorno, J., McKrell, T., Hu, L.-W., Rubner, M., and Cohen, R., 2013, "Separate Effects of Surface Roughness, Wettability, and Porosity on the Boiling Critical Heat Flux," Appl. Phys. Lett., 103(2), p. 024102.

[27] Rahman, M. M. Olceroglu, E., and McCarthy, M., 2014, "Role of Wickability on the Critical Heat Flux of Structured Superhydrophilic Surfaces," Langmuir, 30(37), pp. 11225–11234.

[28] Berber, S., Kwon, Y.-K., and Tománek, D., 2000, "Unusually High Thermal Conductivity of Carbon Nanotubes," Phys. Rev. Lett., 84(20), p. 4613.

[29] K. S. Novoselov, A. K. Geim, S. V. Morozov, D. Jiang, Y. Zhang, S. V. Dubonos, I. V. Grigorieva, and A. A. Firsov, "Electric Field Effect in Atomically Thin Carbon Films," *Science*, vol. 306, no. 5696, pp. 666–669, Oct. 2004.

[30] Jaikumar, A., Santhanam, K. S. V., Kandlikar, S. G., Raya, I. B. P., and Raghupathi, P., 2015, "Electrochemical Deposition of Copper on Graphene with High Heat Transfer Coefficient," ECS Trans., 66(30), pp. 55–64.

[31] Protich, Z., Santhanam, K. S. V., Jaikumar, A., Kandlikar, S. G., and Wong, P., 2016, "Electrochemical Deposition of Copper in Graphene Quantum Dot Bath: Pool Boiling Enhancement," J. Electrochem. Soc., 163(6), pp. E166–E172.

[32] Park, S. D., Won Lee, S., Kang, S., Bang, I. C., Kim, J. H., Shin, H. S., Lee, D. W., and Won Lee, D., 2010, "Effects of Nanofluids Containing Graphene/Graphene-Oxide Nanosheets on Critical Heat Flux," Appl. Phys. Lett., 97(2), p. 023103.

[33] Ahn, H. S., Kim, J. M., Kaviany, M., and Kim, M. H., 2014, "Pool Boiling Experiments in Reduced Graphene Oxide Colloids. Part I Boiling Characteristics," Int. J. Heat Mass Transf., 74, pp. 501–512.

[34] Ahn, H. S., Kim, J. M., Kaviany, M., and Kim, M. H., 2014, "Pool Boiling Experiments in Reduced Graphene Oxide Colloids Part II – Behavior after the CHF, and Boiling Hysteresis," Int. J. Heat Mass Transf., 78, pp. 224–231.

[35] Kim, J. M., Kim, T., Kim, J., Kim, M. H., and Ahn, H. S., 2014, "Effect of a Graphene Oxide Coating Layer on Critical Heat Flux Enhancement under Pool Boiling," Int. J. Heat Mass Transf., 77, pp. 919–927.

[36] Mejia V., "Pool Boiling Heat Transfer Surface Enhancement using Electrodeposition with Non-Electrolyte Bath" (2015). Thesis, Rochester Institute of Technology,

[37] Raj, R., Maroo, S. C., and Wang, E. N., 2013, "Wettability of Graphene," Nano Lett., 13(4), pp. 1509–1515.

[38] Jaikumar, A., and Kandlikar, S. G., 2015, "Enhanced Pool Boiling Heat Transfer Mechanisms for Selectively Sintered Open Microchannels," Int. J. Heat Mass Transf., 88, pp. 652–661.

[39] Bard, A. J., and Faulkner, L. R., 2002, *Fundamentals and Applications, New York: Wiley, 2001*, Springer.

[40] "Faraday_laws_of_electrolysis.pdf."

[41] Patil, C., 2014, *Enhancement of Pool Boiling Heat Transfer Using a Combination of Open Microchannels and Microporous Surfaces*, Rochester Institute of Technology.

[42] Mejia V., "Pool Boiling Heat Transfer Surface Enhancement using Electrodeposition with Non-Electrolyte Bath" (2015). Thesis, Rochester Institute of Technology, Accessed from, http://scholarworks.rit.edu/theses/8632

[43] Jaikumar, A., Rishi, A., Gupta, A., and Kandlikar, S. G., 2017, "Microscale Morphology Effects of Copper–Graphene Oxide Coatings on Pool Boiling Characteristics," J. Heat Transf., 139(11), pp. 111509-111509–11.

[44] Liu, F., 2016, *A Study of Sintered Copper Porous Surfaces for Pool Boiling Enhancement*, Rochester Institute of Technology.

[45] Zou, A., and Maroo, S. C., 2013, "Critical Height of Micro/Nano Structures for Pool Boiling Heat Transfer Enhancement," Appl. Phys. Lett., 103(22), p. 221602.

[46] Hafner, B., 2007, "Scanning Electron Microscopy Primer," Charact. Facil. Univ. Minn.-Twin Cities, pp. 1–29.

[47] 2015., ز, نوفل, "Infrared Spectroscopy," 1, حلقات البحث(6).

[48] Drewniak, S., Muzyka, R., Stolarczyk, A., Pustelny, T., Kotyczka-Mora?ska, M., and Setkiewicz, M., 2016, “Studies of Reduced Graphene Oxide and Graphite Oxide in the Aspect of Their Possible Application in Gas Sensors,” Sensors, 16(1), p. 103.